Lunar Pole Illumination and Communications Statistics Computed from GSSR Elevation Data

Scott Bryant[1]
California Institute of Technology, Jet Propulsion Laboratory, Pasadena, CA, 91109

The Goldstone Solar System RADAR (GSSR) group at JPL produced a Digital Elevation Model (DEM) of the lunar south pole using data obtained in 2006. This model has 40-meter horizontal resolution and about 5-meter relative vertical accuracy. This paper uses that Digital Elevation Model to compute average solar illumination and Earth visibility near the lunar south pole. This data quantifies solar power and Earth communications resources at proposed lunar base locations. The elevation data were converted into local terrain horizon masks, then converted into selenographic latitude and longitude coordinates. The horizon masks were compared to latitude, longitude regions bounding the maximum Sun and Earth motions relative to the moon. Proposed lunar south pole base sites were examined in detail, with the best site showing multi-year averages of solar power availability of 92% and Direct-To-Earth (DTE) communication availability of about 50%. Results are compared with a theoretical model, and with actual sun and Earth visibility averaged over the years 2009 to 2028. Results for the lunar North pole were computed using the GSSR DEM of the lunar North pole produced in 1997. The paper also explores using a heliostat to reduce the photovoltaic power system mass and complexity.

I. Introduction

Because of the 1.54-degree inclination of the moon's rotation pole to the Ecliptic plane, the sun never rises more than a few degrees of elevation angle above the horizon at the lunar polar regions. Many depressions and crater floors near the poles are permanently shaded from the sun, producing a permanent low-temperature area. These permanently shaded areas may be reservoirs for water ice deposits[1]. The potential for using lunar ice to produce oxygen, hydrogen fuel, and drinking water is driving investigations of human exploration bases at the lunar poles[2].

The same geometry that creates permanently shadowed regions in lunar polar craters also increases solar illumination on lunar polar mountains. A typical lunar surface location is exposed to the sun for half of the 29.5-day synodic month. But a tall peak near the lunar poles could view the sun during the entire synodic month. These "Peaks of Eternal Light"[3] would provide base sites with near-continuous solar power and illumination[4, 5]. The analysis presented here expands on previous results[6] to show there is no Peak of Eternal Light at either lunar pole. The results do show locations with more than 90% solar illumination when averaged over several lunar years.

Evaluating the resource potential of lunar polar base sites is a high priority for future lunar exploration[7]. This includes determining the amount of Direct-To-Earth (DTE) communications available from the polar base locations. The orbital mechanics causing the lunar librations seen from Earth also cause the Earth to move across several degrees of elevation and azimuth in the lunar sky. Even though the moon is tidally locked, the Earth appears to move $\pm$ 6.87 degrees in latitude and $\pm$ 8.16 degrees in longitude[2]. Therefore, lunar polar base DTE communications is only possible about half of each Sidereal Month (27.3 days). This paper presents multi-year averages of solar illumination, solar power, and Earth visibility metrics for the lunar pole regions to help evaluate base sites.

---

[1] Telecommunications Engineer, Section 333, 4800 Oak Grove Drive/Mailstop 238-737.

[2] R. Roncoli, "Lunar Constants and Models Document", JPL D-32296 (internal document), Jet Propulsion Laboratory, Pasadena, California, Sept 23, 2005.

II. Background

The latest Goldstone Solar System Radar (GSSR) DEM was produced by the GSSR group at JPL from observations taken during September 2006. The GSSR group uses antennas in NASA's Deep Space Network to produce radar images of solar system objects[8] using interferometry techniques. These data were acquired during lunar librations that increased the view of the lunar South pole. The Earth's selenographic latitude during the data acquisition was 6.2 degrees South, allowing the GSSR to see lunar terrain several degrees toward the Farside of the lunar South pole. The GSSR group processed the radar data into a DEM in lunar polar stereographic projection coordinates. The DEM covers an area approximately 880 km from Nearside to Farside and 500 km East to West across the lunar South pole. The DEM covers the lunar South pole, out to 70 km toward the lunar Farside and farther in the other directions.

The DEM uses a polar stereographic Cartesian coordinate system centered on the lunar South pole, with X-axis pointed East (90 degrees lunar East Longitude), and Y-axis pointed Nearside (0 degrees lunar East Longitude). Figure 1 shows the lunar South pole region of the 2006 DEM data, along with some lunar features. The lunar South pole is on the rim of Shackleton crater. Figure 2 shows the lunar North pole region of the 1997 Digital Elevation Model data, with some lunar features. The gray areas in both figures were not visible from the Earth during the RADAR imaging. Both figures show two-letter designations of proposed base sites used in this paper. The base site lettering is derived from the base site identification used in Reference 4. Most features names and locations are from the International Astronomical Union (IAU) lunar naming in the Gazetteer of Planetary Nomenclature[3], however some of the mountain peaks use older, unofficial names[9].

Figure 3 shows the proposed lunar South pole base locations around Shackleton crater. The figure reveals the high resolution of the 2006 South pole RADAR DEM. The 40-meter spatial resolution of the data produces a topographic map with good internal consistency and rich detail.

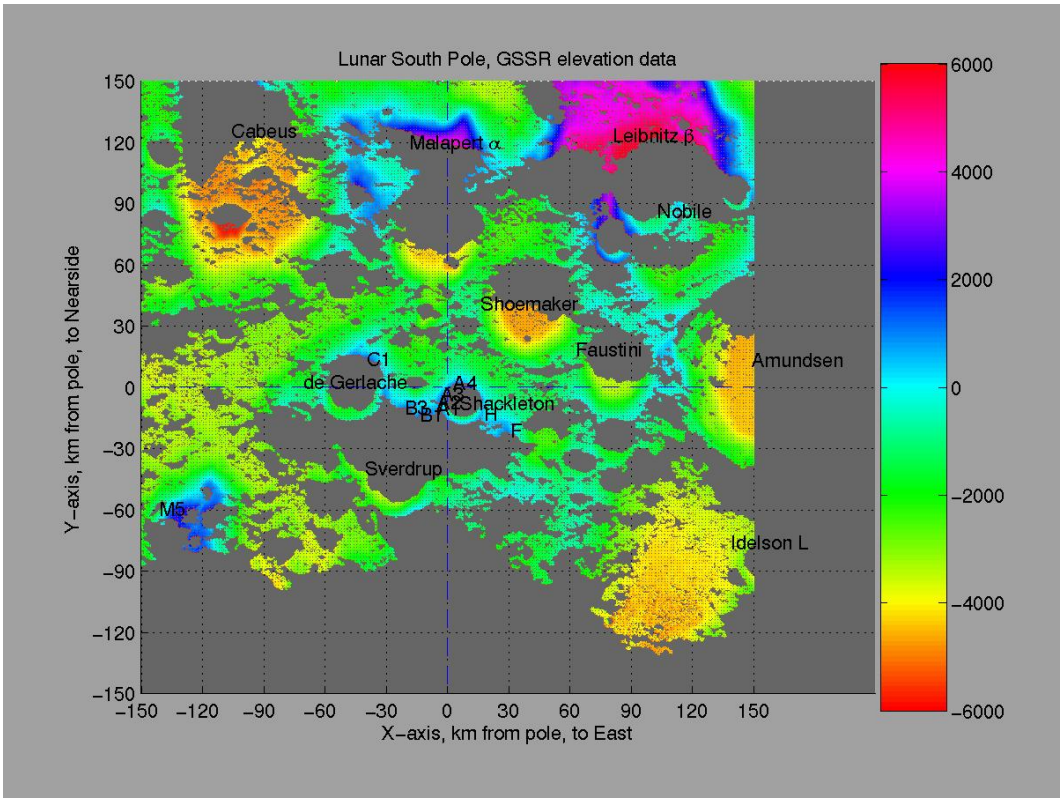

Figure 1. Lunar South Pole Elevation Map from GSSR 2006 Digital Elevation Model.

[3] International Astronomical Union, IAU Gazetteer of Planetary Nomenclature. http://planetarynames.wr.usgs.gov

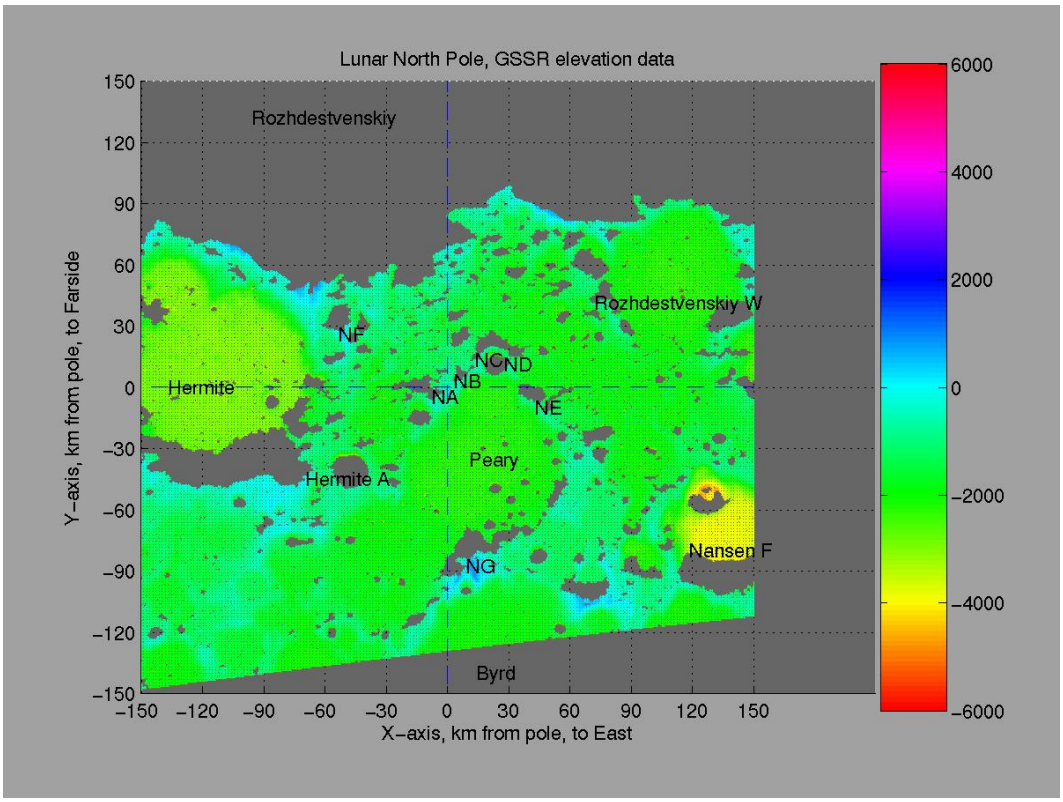

Figure 2. Lunar North Pole Elevation Map from GSSR 1997 Digital Elevation Model.

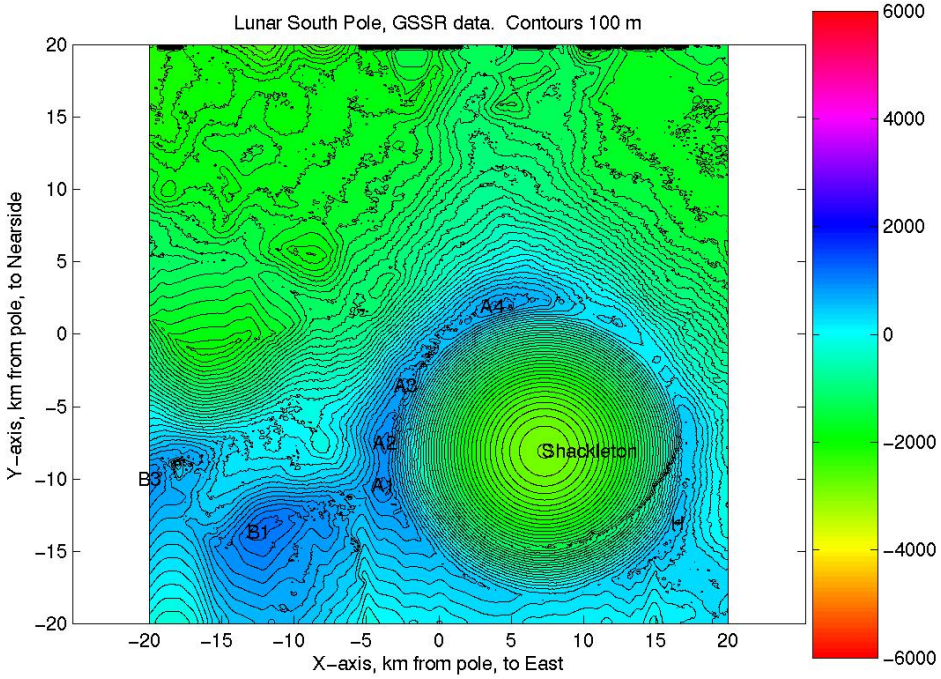

Figure 3. Shackleton Crater Topographic Map, with Base Sites.

Inside Shackleton crater, the missing elevation data within the RADAR shadow were filled in with values based on a parabolic elevation profile. Figure 3 also indicates the rim of Shackleton crater covers a horizontal distance of about 200 meters (5 data points), instead of being an abrupt scarp. This suggests the actual Digital Elevation Model point-to-point elevation error is close to the stated relative vertical accuracy of 5 meters[8]. Based on this vertical accuracy, the analysis used 2-meter tall towers for the baseline horizon mask computations.

Table 1 lists lunar pole features and their locations in both lunar coordinate systems. Some feature names are not official International Astronomical Union (IAU) names[9]. Crater locations are for the apparent center of the crater. Proposed base site locations are given later in this paper.

Table 1. Lunar North and South Pole feature coordinates.

Feature	Pole	X km	Y km	Lat.	Long.	Crater diameter or Mountain elevation, km
Malapert α	S	3.56	119.60	-86.037	1.705	4.207
Leibnitz β	S	101.32	123.04	-84.723	39.471	6.055
M5	S	-134.95	-59.97	-85.110	-113.960	2.557
Amundsen Crater	S	171.67	13.21	-84.300	85.600	156.000
Cabeus Crater	S	-89.45	125.40	-84.900	-35.500	98.000
de Gerlache Crater	S	-45.22	2.29	-88.500	-87.100	32.400
Faustini Crater	S	79.42	18.34	-87.300	77.000	39.000
Idelson L Crater	S	157.74	-76.26	-84.200	115.800	28.000
Malapert Crater	S	34.39	150.14	-84.900	12.900	69.000
Nobile Crater	S	116.53	86.22	-85.200	53.500	73.000
Shackleton Crater (from GSSR values)	S	7.32	-8.08	-89.639	137.825	19.000
Shackleton Crater (IAU values)	S	0.00	3.02	-89.900	0.000	19.000
Shoemaker Crater	S	40.48	40.62	-88.100	44.900	50.900
Sverdrup Crater	S	-21.26	-39.98	-88.500	-152.000	35.000
Byrd	N	24.16	-139.86	85.300	9.800	93.000
Hermite	N	-120.78	-0.21	86.000	-89.900	104.000
Hermite A	N	-48.65	-45.21	87.800	-47.100	20.000
Nansen F	N	138.63	-80.04	84.700	60.000	62.000
Peary	N	23.01	-35.44	88.600	33.000	73.000
Rozhdestvenskiy	N	-60.34	131.80	85.200	-155.400	77.000
Rozhdestvenskiy W	N	113.49	41.31	86.000	110.000	75.000

III. Analysis Method

Analyzing the DEM to produce solar illumination and DTE communications required several major steps. Step 1 corrected the DEM elevations, by removing bad points and filling in radar shadow areas with approximate elevations. Step 2 computed horizon masks from the DEM information. Topocentric horizon masks were computed for a viewpoint at 2 meters altitude above the surface, and then converted into selenographic (lunar-centered) equatorial latitude and longitude coordinates. Step 3 estimated multi-year average illumination metrics by comparing the horizon mask in selenographic latitude and longitude to a uniform distribution of the sun and Earth exposure in selenographic coordinates. This step assumed a simplified time average for the solar and Earth motions as seen from the moon, eliminating the astrodynamics calculations. Step 4 collected these multi-year average illumination and DTE visibility metrics for areas around the lunar South pole. Those metrics are presented as contour plots, tables, and horizon masks.

The analysis was then extended using actual Sun and Earth positions, as seen from the lunar poles. The multi-year average illumination and DTE metrics were computed using actual sun and Earth positions for the years 2009 to 2028. In addition, a theory was developed for multi-year average illumination and DTE visibility as a function of

lunar location and altitude above the lunar surface. The metrics from step 3 and the metrics using actual positions were then recomputed for several heights above the lunar surface, and compared with the developed theory.

A. Step 1: Correcting DEM Elevation and Filling Radar Shadows

During the 2006 GSSR data acquisition, the Earth was at about 6.2 degrees South selenographic latitude. This placed Earth at approximately +6.2 degrees of elevation angle as seen from the lunar South pole. Therefore, some parts of the polar terrain were not visible to the radar. For the 100 km x 100 km area centered on the lunar South pole, about 40% of the area was not imaged because it was in radar shadow. In addition, several imaged areas had very low radar backscatter signal strength, leading to spurious elevation values. Several locations next to the radar shadow edge have erroneous elevation values. These features of the GSSR DEM required correction prior to using the DEM for illumination computations.

Matlab was used for most of the computation, including the data corrections. First, the 2006 GSSR DEM file of elevations and the file of backscatter magnitudes were read into Matlab. Because of the large file size, the program read a data subset covering100 km x 100 km area at full 40-meter resolution (2501 x 2501 pixels) centered on the lunar South pole. For coarser far-field computations, the program read in a 400 km x 400 km area and decimated it to 600-meter resolution by taking every 15^{th} point (667 x 667 pixels). The program then edited the DEM elevations to remove known artifacts. Specifically, the areas (-8.5 km < X < -7 km, -14.5 km < Y < -13.5 km) and (-7 km < X < -3 km, -16 km < Y < -12 km) were scanned and all elevations greater than 800 meters were set to the value of the radar shadow areas (-10,000 meters). This removed 2 steep-sided 'towers' on a ridgeline West of Shackleton crater. GSSR experts at JPL confirmed these 2 'towers' were probably anomalies from the elevation processing algorithms. The remaining area was 6,180 km^2, or 61.8% of the 100 km x 100 km original area.

The Matlab program then pruned out elevations with local slopes in excess of 60 degrees. For the 100 km x 100 km area centered on the lunar South pole, this removed 1.7% of the remaining elevation area. Next the program removed elevation points with radar backscatter value less than 0.06%. For the 100 km x 100 km area, this removed 18.3% of the remaining elevation area. Several elevation anomalies were eliminated by these slope and backscatter limits, including hilly terrain inside the Nearside-East rim of Shackleton crater. This hilly terrain was determined to be a processing artifact, because it would have obscured the Earth's view of other radar-imaged terrain inside Shackleton crater.

The Matlab program then scanned the remaining elevation values and removed any points with less than 4 surrounding points. This removed almost all small 'islands' of isolated elevation data, which had proven to be mostly artifacts of the radar processing. This step removed 0.5% of the elevation data. The cumulative effect of the data editing removed about 21% of the original elevation data in the 100 km x 100 km map. This reduced the elevation data coverage from 6180 km^2 to 4916 km^2 or from 61.8% to 49.2% of the 100 km x 100 km map. Similar percentages were removed for the larger coarse maps.

The Matlab program then created elevation data to fill in the missing points. Inside Shackleton crater, the program created a parabolic surface with a center elevation of -2900 meters at X = 7.32 km, Y = -8.08 km. This produced a more realistic 3 dimensional plot of the crater, but did not affect the illumination results. For the remaining radar shadow and edited areas, the program set the elevation values to the altitude of the radar shadow. The program scanned each column of elevation data from the +Y to –Y direction. At each missing data location, the program computed a straight line from Earth at 6.2 degrees South selenographic latitude that passed through the last known +Y elevation data value. This means the elevation in the unknown terrain was set to values just under the GSSR radar shadow envelope. This models an upper bound on the possible elevations. If the actual elevations were higher, then the point would have appeared on the radar. This upper bound provides a conservative estimate for solar illumination computations. Actual terrain elevations inside the radar shadow area are probably lower than the radar line of sight, and would block less of the surrounding terrain. The program also set a lower limit of -5000 meters elevation to prevent elevation estimates toward the lunar Farside from becoming excessively deep.

Similar pruning was applied to the lunar North pole Digital Elevation Model from 1997. The Matlab program read in a 400 km x 400 km area at the 600-meter resolution of the Digital Elevation Model. The same data pruning algorithms were applied, but no specific elevation artifacts were targeted for removal.

B. Step 2: Horizon Mask Computation

The horizon masks were computed by scanning along lines of constant azimuth. For convenience in computation, the line of 0 azimuth was always parallel to the Lunar prime meridian at 0 degree longitude, not due North. This made the conversion to the final equatorial coordinates easier and did not affect the results. Maps were selected with "coarse" or "fine" grid resolution, as described below. For each point on the grid, the Matlab program

defined a circle around the point, then scanned along lines of azimuth for at least 200 km. This 200 km distance was determined from a requirement to examine far enough along the azimuth lines to find any peaks that would block the sun. At mid-Winter, the sun will be at an elevation angle of -1.54 degrees as seen from the lunar South pole. The tallest peak near the lunar South pole is Leibnitz β, at an elevation of 6055 meters. As shown in Figure 4, the lunar horizon falls off quickly with distance. The plot indicates that at 200 km from the pole, a mountain must be over 7000 meters tall in order to block the Winter sun. This gave a practical limit of 200 km for the distance to use in examining the lines of azimuth. This also set the size necessary for the DEM subsets around the lunar pole.

The elevation angles were computed starting at the grid point at the center of the horizon mask and extending out to points on the lunar terrain along each azimuth line. The maximum elevation angle for each azimuth was stored in an array of horizon mask elevation versus azimuth. The horizon mask results depend on the altitude of the observer at the horizon mask center. Unless otherwise stated, an observation tower 2 meters above the local terrain was used for the horizon mask computations. This represented a practical height for solar array installation. For some locations, additional horizon mask metrics were computed using taller towers.

Coarse resolution horizon masks were computed from a DEM decimated to 600-meter spatial resolution that extended ±200 km around the lunar South Pole. The lines of azimuth were spaced 5 degrees apart. Maps were generated covering 30 km x 30 km areas (51 by 51 pixels). A total of 64 maps were generated to cover the region within 110 km of the lunar South pole. For the lunar North pole, maps were generated in the same way. Because there are no extremely tall mountains to consider near the lunar North pole, fewer maps were examined. A total of 42 maps were generated, covering the regions within 105 km of the lunar North pole, except the Farside, which was covered to 75 km.

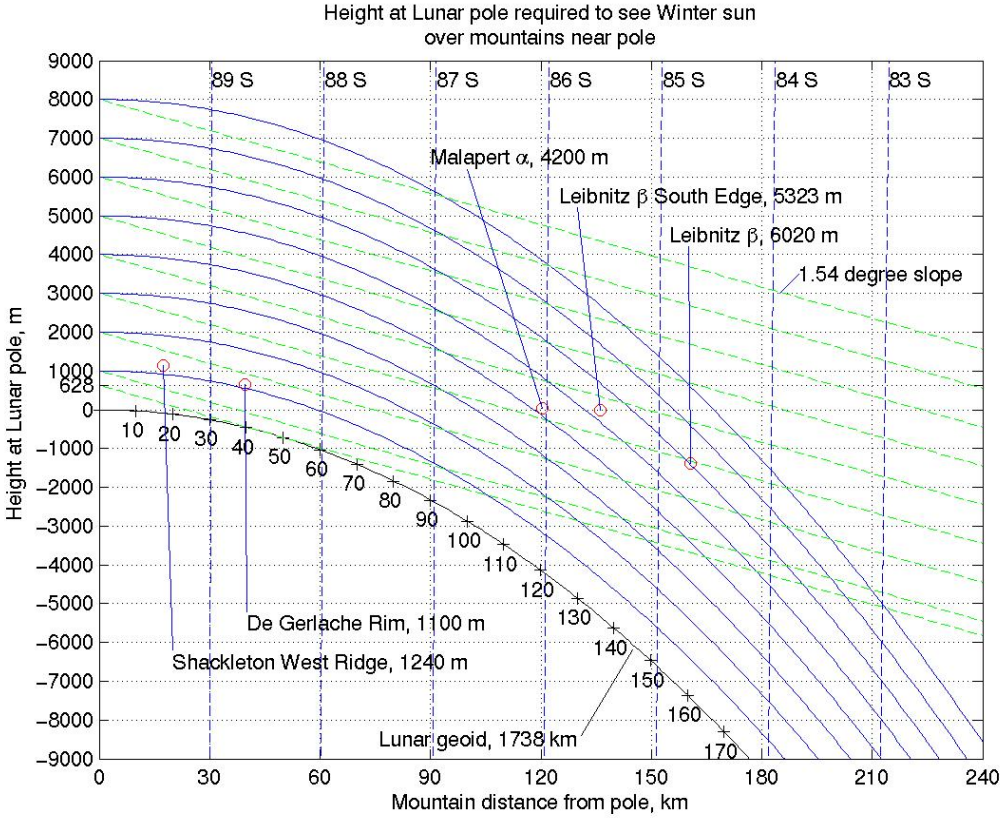

Figure 4. Solar Lines-of-Sight at Lunar South Pole.

For the lunar South pole, medium resolution horizon masks were computed for specific areas of interest identified from the coarse resolution maps. The medium resolution masks used 2 Digital Elevation Models: a coarse Digital Elevation Model decimated to 1000-meter spatial resolution that extended ±200 km around the lunar South pole, and a fine Digital Elevation Model at 40-meter spatial resolution that extended ±6 km around the location of interest. This 12 km x 12 km area was removed from the coarse Digital Elevation Model prior to the elevation angle

computations. Horizon masks were computed for both Digital Elevation Models, using azimuth spacing of 5 degrees. Then for each azimuth, the greater elevation angle of the 2 horizon masks was selected for the composite horizon mask. This 2 Digital Elevation Model approach produced a higher resolution result, while keeping the computation time reasonably short. Maps were generated covering 1 km x 1 km areas with resolution of 40 meters (51 by 51 pixels).

For a small number of locations, fine resolution horizon masks were computed using 2 Digital Elevation Models: a coarse Digital Elevation Model decimated to 1000 meter spatial resolution that extended $\pm$200 km around the lunar South pole, and a fine Digital Elevation Model at 40 meter spatial resolution that extended $\pm$50 km around the lunar South pole. This 100 km x 100 km area was removed from the coarse Digital Elevation Model prior to the elevation angle computations. Horizon masks were computed for both Digital Elevation Models, using azimuth spacing of 1 degree. Then for each azimuth, the greater elevation angle of the 2 horizon masks was selected for the composite horizon mask. This 2 Digital Elevation Model approach produced a higher resolution result, while keeping the computation time reasonably short. Horizon masks were computed for single point locations, and extra solar illumination and Earth visibility metrics were created from the horizon masks. The fine resolution computations were performed only at locations with high solar illumination found from the coarse and medium resolution maps.

C. Step 3: Computing Illumination Metrics from Average Solar and Earth Motion

Figure 5 shows a horizon mask profile in lunar topographic azimuth and elevation coordinates. This mask was produced with 1-degree azimuth steps using the 'Fine' resolution technique described above. The figure shows areas defining the limits for the Earth and solar motion, as seen from the moon. In selenographic coordinates, the Earth's center is confined to a maximum East-West longitude libration of 8.16 degrees, and a North-South latitude libration of 6.87 degrees[2]. These librations values are the maximum possible librations, not the typical average values. In selenographic coordinates, the maximum excursion of the Earth's center is shown by the parallelogram marked with red circles. The Earth's disk subtends an angle of 1.9 degrees, as seen from the moon. Therefore the limbs of the Earth will extend beyond the box defined above. The limits of the motion of Earth's South Pole are shown by the parallelogram marked with red upward-pointing triangles. The limits of the motion of Earth's North Pole are shown by the parallelogram marked with red downward-pointing triangles.

The sun moves across all degrees of longitude, but is confined to latitudes between 1.54 degrees North and South. The motion of the Sun's center is plotted with yellow circles. The solar disk subtends an angle of 0.53 degrees, as seen from the moon. The motion of the Northern and Southern limbs of the sun are shown with yellow lines. The boundary limit of the solar path is lowest on the horizon in the direction of the lunar South pole, at azimuth = arctan(x/y) or 42.2 degrees. Note the sinusoidal shape of the solar limits in the azimuth-elevation coordinate frame of figure 5. This sinusoidal shape is due to the coordinate transformation from selenographic latitude-longitude, to a local topocentric frame centered away from the lunar pole. In this local topocentric frame, lines of constant selenographic latitude are not lines of constant elevation.

Figure 6 shows the same information as Figure 5, but expressed in selenographic coordinates. The selenographic coordinate frame has 0 degrees of latitude in directions parallel to the lunar equator, and 0 degrees of longitude in directions parallel to the Nearside prime meridian facing Earth. In the selenographic coordinate frame, the Earth and Sun maximum limits are defined by rectangles of constant latitude and longitude. Note that Figure 6 defines South latitude as positive, so that the lunar terrain horizon mask for this lunar South pole location appears "right side up" when compared to figure 5. Figure 6 shows the lunar terrain horizon mask has shifted with the transformation to selenographic coordinates, raising up in the direction of the lunar South pole at 42.2 degrees longitude, and dipping down in the direction of the lunar North pole at -137.8 degrees longitude.

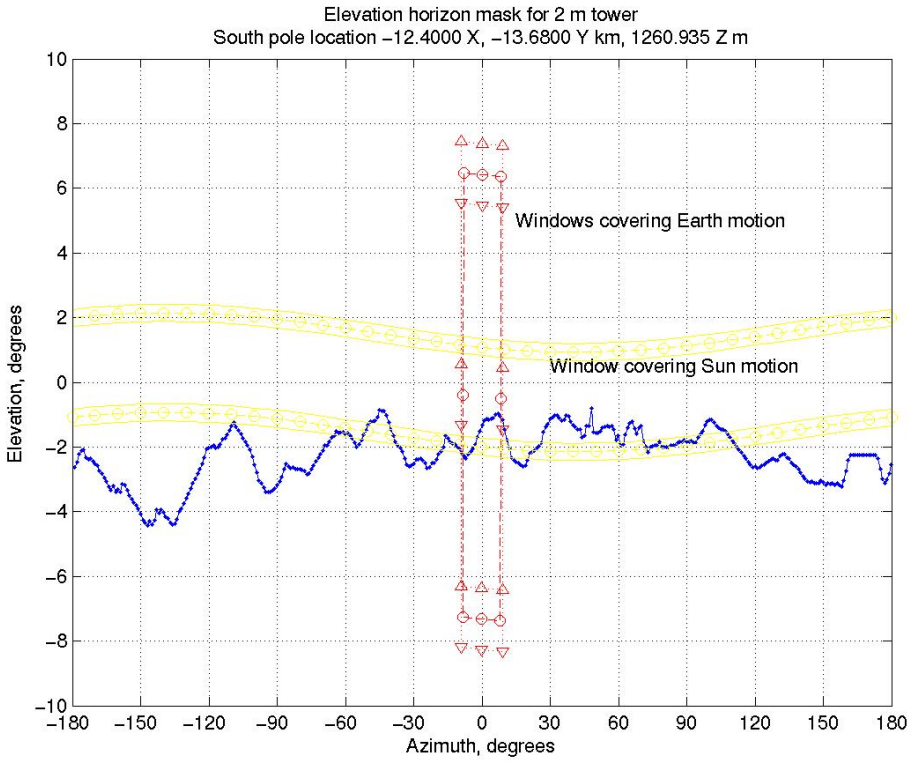

Figure 5. Site B1 Terrain horizon mask with 1 degree azimuth spacing.

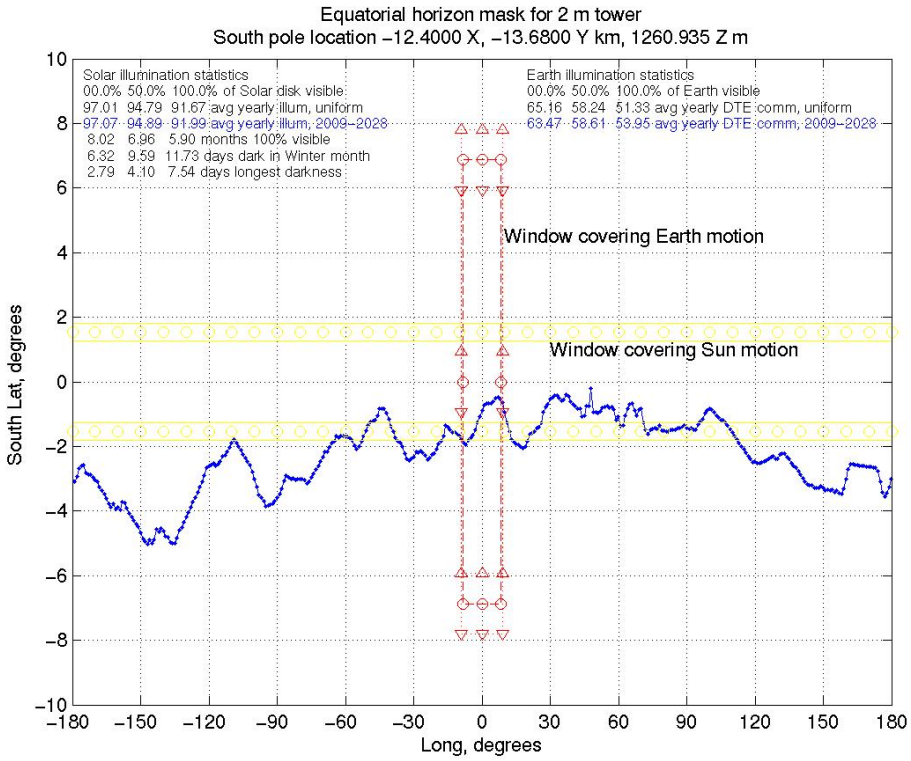

Figure 6. Site B1 Terrain horizon mask with 1 degree azimuth spacing, in selenographic coordinates.

The following assumptions were made to simplify computing multi-year averages of the solar illumination and Earth visibility:

1) In selenographic coordinates, the center of the Sun and Earth stay inside the bounding rectangles defining the maximum longitude and latitude excursions. The center of the solar disk stays within a rectangle defined by East-West longitudes180 degrees, and North-South latitudes of 1.54 degrees. The center of Earth's disk stays within East-West longitudes 8.16 degrees, and North-South latitudes 6.87 degrees.

2) Averaged over many years, the Sun and Earth motions bring them to all locations within their bounding rectangles. Particularly, during the 18.6-year period of the regression of the longitude of the ascending node, the Earth will cover all locations within its bounding rectangle.

3) Averaged over many years, the Sun has an equal probability at being at any location within its bounding rectangle. A similar assumption is made for the Earth within its bounding rectangle. This assumption is less accurate for the Earth, since the Earth does not reach the extremes of latitude libration in every year.

These assumptions bypass computing the exact location of the Sun and Earth at specific times of interest. Instead, the illumination computations use the area of the bounding rectangles in Figure 6. Assumptions 1 and 2 were verified using data computed using the Jet Propulsion Laboratory (JPL) HORIZONS on-line solar system data and ephemeris computations service[4]. Figures 7 and 8 use data computed for an observer at the lunar South pole with data points every 24 hours. Figures 7 and 8 define North latitude as positive.

Figure 7 shows the view of the sun in selenographic latitude and longitude for the period January 1, 2009 to January 1, 2010. The black circles show the disk of the sun centered on the blue cross of each data point.

Figure 8 shows the view of the Earth in selenographic latitude and longitude for the period January 1, 2009 to January 1, 2010. The black circles show the disk of the Earth centered on the blue cross of each data point. The red rectangle shows the assumed bounding rectangle of the center of Earth's disk within East-West longitudes 8.16 degrees, and North-South latitudes 6.87 degrees. Over the year 2009, the Earth does not cover the entire bounding rectangle, but traces an approximation to a Lissajous curve between the lower left and upper right corners. These figures indicate that assumptions 1 and 2 agree with the actual ephemeris data. The assumption of a uniform distribution across the bounding rectangle is examined in more detail later in this paper.

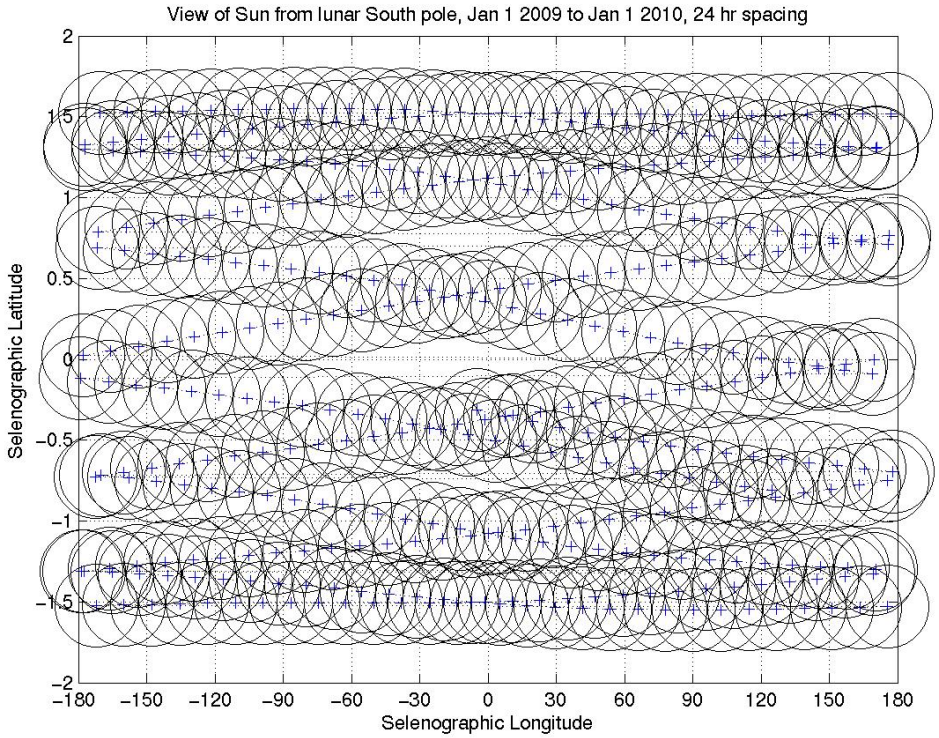

Figure 7. Lunar South Pole Ephemeris Data for the Sun, 2009 to 2010.

4 JPL HORIZONS. http://ssd.jpl.nasa.gov/?horizons

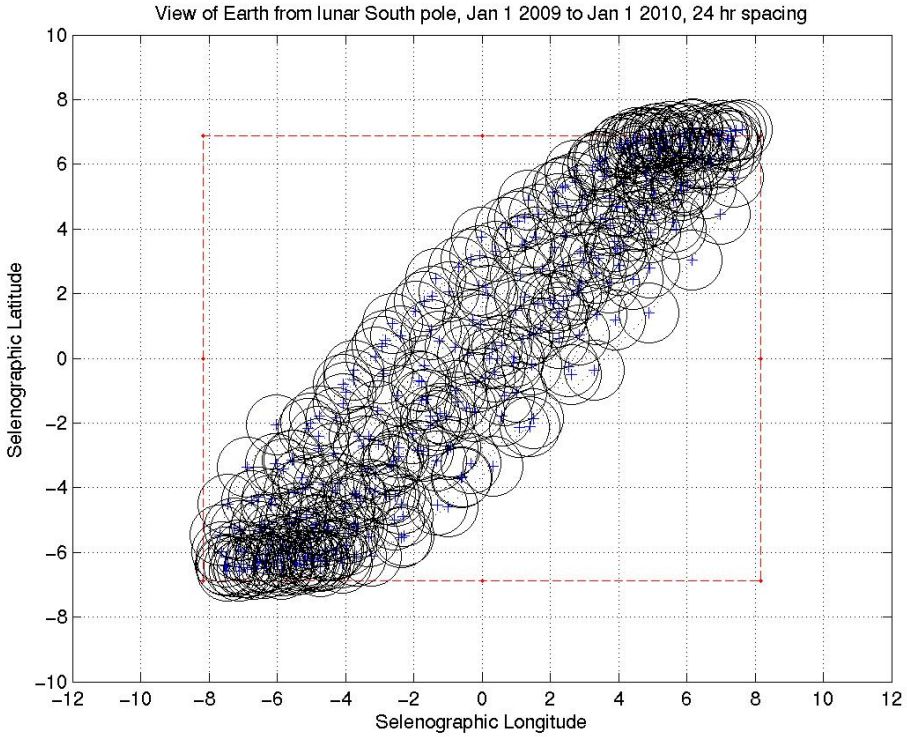

Figure 8. Lunar South Pole Ephemeris Data for the Earth, 2009 to 2010.

The illumination metrics in the next step are based on how much area of the bounding rectangle is covered by the terrain horizon mask. The assumptions 1 through 3 mean that the illumination metrics will not be exact for a particular date, but will represent a multi-year average value. These averaged values allow comparisons between different lunar sites, since the only variable is the lunar terrain at the different locations. These assumptions greatly reduced the amount of computation needed for computing illumination and Earth visibility metrics.

D. Step 4: Collecting Solar Illumination and DTE Visibility Metrics

Based on the assumptions above, several metrics were computed from horizon masks projected into the lunar selenographic coordinates. Average solar illumination was computed by integrating the area of the Sun's bounding rectangle above the horizon mask. The integrated area was then normalized with the area of the entire solar bounding rectangle, resulting in the percentage of time that the sun is visible. Three types of solar illumination averages were computed, varying with the amount of visible solar disk (see Figure 6). Since the solar disk radius is 0.265 degrees as seen from Earth's orbit, the metrics vary with the amount of the solar disk covered.

The "0% of solar disk visible" is the average computed by integrating the horizon mask over the solar bounding rectangle from 1.275 degrees North to 1.805 degrees South latitude. Using the convention shown in Figure 6, defining South latitude as positive, this integration from -1.275 degrees to +1.805 degrees latitude. This metric requires that the horizon mask cover the entire solar disk, up to the Southern limb, to not count as illuminating the lunar terrain. This metric represents the amount of time that any solar light is available.

The "50% of solar disk visible" metric integrated the horizon mask over the solar bounding rectangle from -1.54 degrees to +1.54 degrees latitude. This metric requires that the horizon mask cover more than half the solar disk to not count as illuminating the lunar terrain. This metric represents half-strength solar illumination.

The "100% of solar disk visible" metric integrated the horizon mask over the solar bounding rectangle from -1.805 degrees to +1.275 degrees latitude. This metric requires that the horizon mask merely touch the solar disk at the Northern limb, to not count as illuminating the lunar terrain. This 100% metric represents the percentage of the multi-year interval with full solar power available.

The three types of Earth illumination averages were computed in a similar way. The "0% of Earth visible" average integrated the horizon mask over the Earth bounding rectangle from -5.92 degrees to +7.82 degrees latitude.

This metric requires that the horizon mask cover the entire Earth disk, up to the Earth's South Pole, to not count as visible to the lunar terrain. The 0% metric represents the percentage of the multi-year interval with some part of the Earth visible at the tower height.

The "50% of Earth visible" average integrated the horizon mask over the Earth bounding rectangle from -6.87 degrees to +6.87 degrees latitude. This metric requires that the horizon mask cover half the Earth's disk to not count as visible. This metric represents the amount of time that the Earth's Southern hemisphere is visible.

The "100% of Earth visible" average integrated the horizon mask over the Earth bounding rectangle from -7.82 degrees to +5.92 degrees latitude. This metric requires that the horizon mask merely touch the Earth's disk at the Earth's North Pole, to not count as visible. This 100% metric represents the percentage of the multi-year interval with a full Earth visible at the tower height.

Additional metrics were estimated for solar power characterization (See Figure 6). The "months 100% visible" estimates the number of synodic months per year when the specified percentage of solar disk is visible. It was computed by comparing the maximum horizon mask peak latitude to the upper and lower solar bounding rectangle limits. The fraction of the bounding rectangle above the maximum peak latitude represents the fraction of the year with continuous solar power.

The metric "days dark in Winter month" lists the number of days during the lunar South pole Winter with less than the specified percentage of solar disk visible. This was computed by finding the amount of each solar bounding rectangle lower edge that was below the horizon mask, normalizing with 360 degrees, and multiplying by 29.5 days. For the "100% of solar disk visible" rectangle, this metric is approximately the sum of the number of days without full solar power during the Winter synodic month. For the "0% of solar disk visible" metric, this is approximately the sum of the days without any solar light during the Winter synodic month. This metric and the "days longest darkness" do not factor in possible solar eclipses, which can last up to 3.9 hours for a partial eclipse[6].

The metric "days longest darkness" is the longest continuous period with less than the specified percentage of solar disk visible. For the "100% of solar disk visible" value, this metric is the longest continuous period without full solar power. For the "0% of solar disk visible" value, this metric is the longest continuous period without any solar light.

The metrics "days dark in Winter month" and "days longest darkness" can be used to set upper and lower bounds on the power system battery storage requirements. For a worst-case number that ignores recharge rates, battery storage can be based on the "days dark in Winter month" value associated with "100% of solar disk visible". Table 3 shows examples of these metrics.

IV. Results

Results from the coarse (600 meter resolution) horizon mask analysis were assembled in graphical and tabular formats. Contour plots for the lunar South pole region covered from X, Y = -129 km, -114 km to X, Y = +111 km, +126 km using 64 maps of size 30 km x 30 km. The combined maps show multi-year average solar illumination and Earth communications visibility values (see Figures 9 and 10). The boundaries for the Coarse maps were chosen so that the entire Shackleton crater fit within the Coarse map from X, Y = -9 km, -24 km to X, Y = +21 km, +6 km. For the lunar North pole region, coarse maps cover from X, Y = -105 km, -105 km to X, Y = +105 km, +75 km. Figures 11 and 12 show multi-year average solar illumination and Earth communications visibility values.

For both lunar poles, sites with the most solar illumination were compared to illumination peak sites in the references. For the lunar South pole, coarse map sites with more than 80% average solar illumination were then examined with Medium resolution maps covering areas 2 km x 2 km. The Medium resolution maps were used to determine the size of each site across 40 m x 40 m pixels. The location of maximum solar illumination in X and Y was then determined for each site. These "peaks of illumination" were then examined with the Fine horizon mask analysis to verify the illumination results and produce additional metrics.

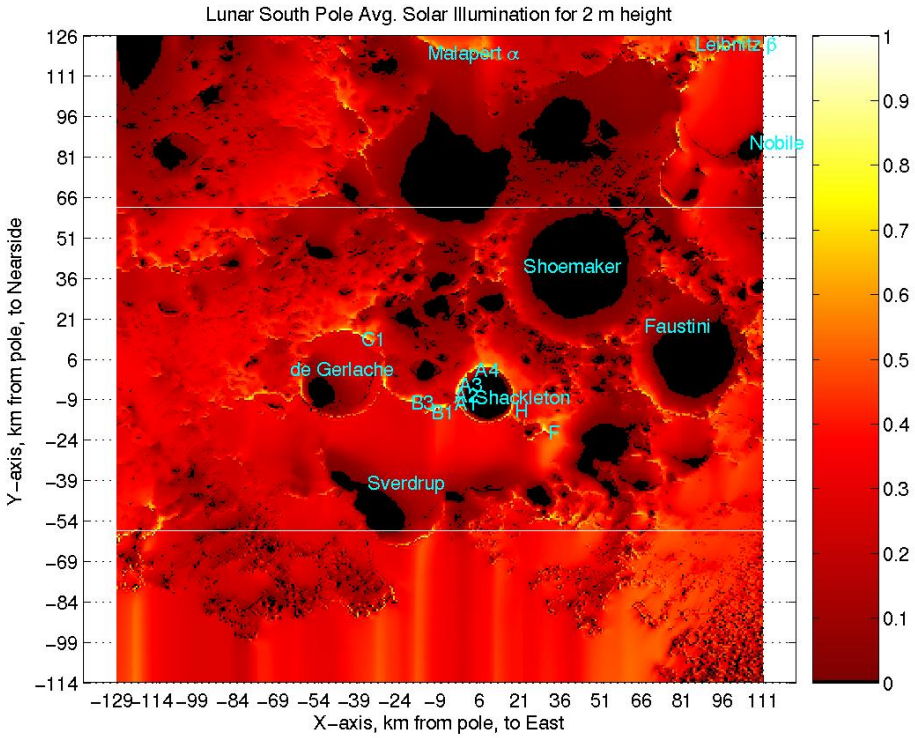

Figure 9. Lunar South Pole Solar Illumination Yearly Average.

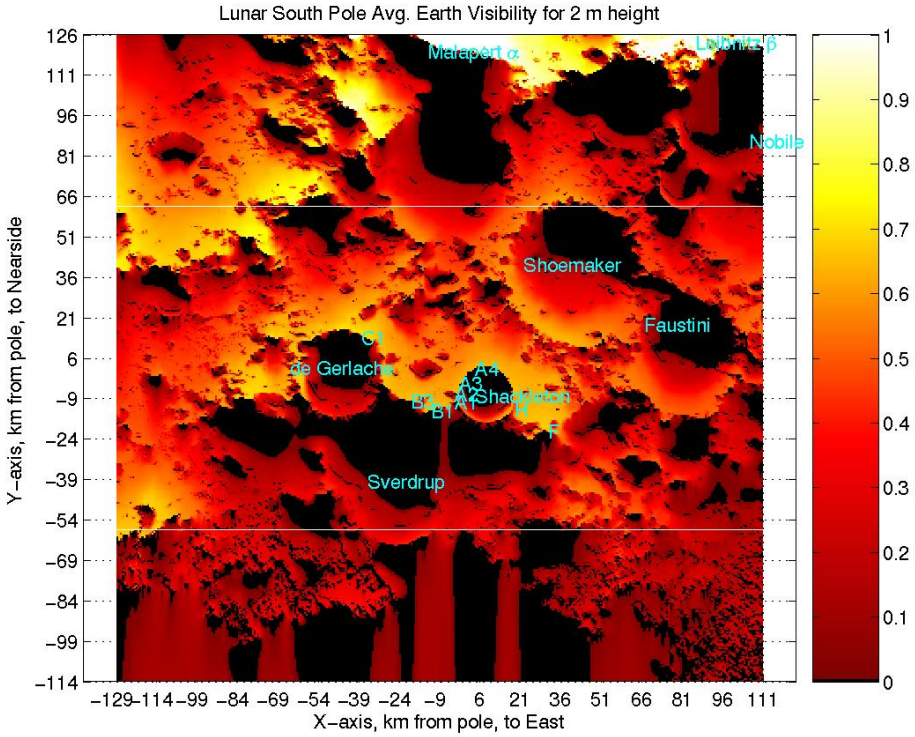

Figure 10. Lunar South Pole DTE Visibility Yearly Average.

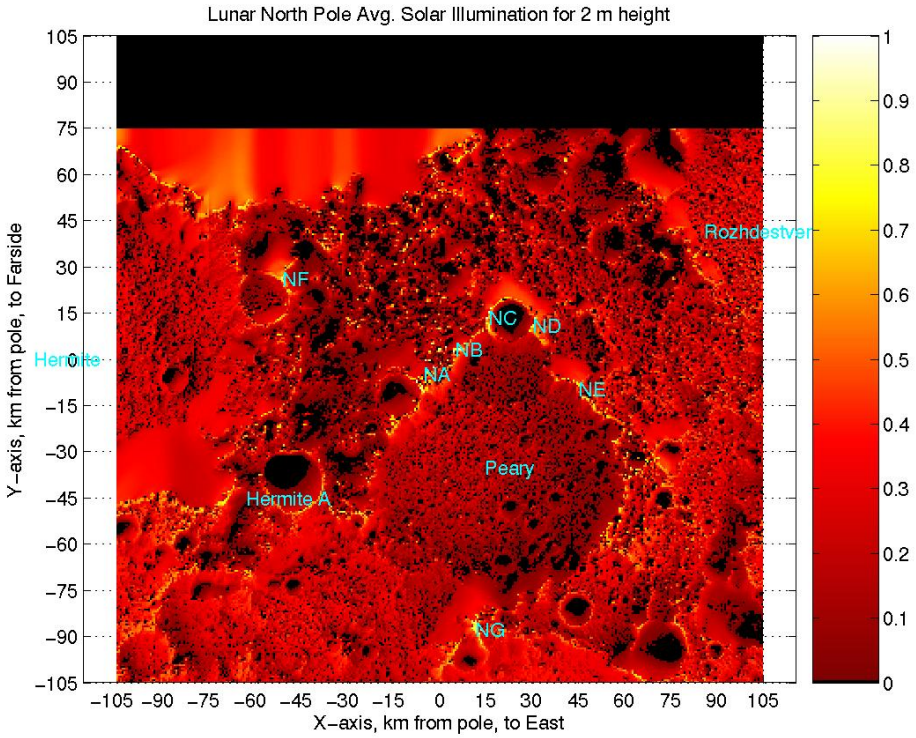

Figure 11. Lunar North Pole Solar Illumination Yearly Average.

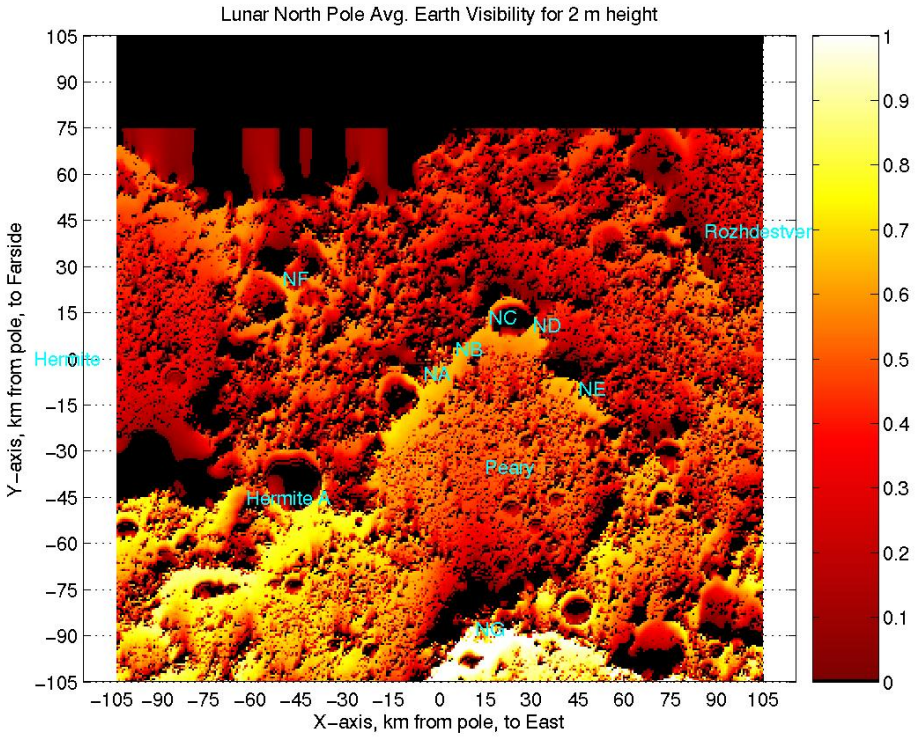

Figure 12. Lunar North Pole DTE Visibility Yearly Average.

A. Coarse Horizon Mask Results

For the South pole region, only 5 of the 64 coarse (30 km x 30 km) maps have peaks with more than 80% average solar illumination. These 5 maps cover the areas:

1) Shackleton crater and the lunar South pole
2) The East ridge from Shackleton crater
3) The West ridge from Shackleton crater
4) The Nearside-East rim of de Gerlache crater
5) The Nearside rim of de Gerlache crater

Figure 13 shows the topographic elevation contours for Shackleton crater. Figure 14 is the same area covered with solar and Earth illumination contours from the coarse horizon mask analysis. The solar illumination contours are every 10% and at 0.0001%. Earth illumination contours are at 0.0001, 0.1, 0.3, 0.5, 0.6, and 0.7%. The illumination data are for any part of the disk visible, or the "0% of solar/Earth disk visible" multi-year average illumination.

The maps confirm that most of Shackleton crater is in permanent shadow (see figures 9 and 14). The contours of the multi-year average solar illumination show small areas of maximum illumination on Shackleton crater's rim and the West Ridge. The maximum is around 90% of continuous illumination. The contours of Earth illumination show these same areas have a maximum multi-year average Earth visibility about 60%. The figures also confirm the solar illumination peak sites identified in References 3, 4, 5, and 6.

These 5 coarse maps were examined for points with multi-year average solar illumination peaks greater than 80%. Those points that are contiguous were given the same site peak name, matching the site names used in Reference 4, Figure 1. Additional sites not listed in Reference 4 are given the name of the closest Site, followed by a new number, e.g. Site B from Reference 4 is listed here as sites B1, B2, and B3.

The site locations identified this way are shown in Figures 9 and 10. These sites show good correlation with the sites listed in Reference 4, but are much lower in elevation due to the different Digital Elevation Model fitting method. Sites B1, A1, and A2 also match well with the 3 peaks of maximum solar illumination identified from Clementine images in Reference 3.

Figures 11 and 12 show the North pole region. There are 7 sites with multi-year average solar illumination peaks greater than 80%. These 7 sites are marked NA through NG on the figures. The 2 best sites are NB and NC with multi-year average solar illumination above 95%. Site NG toward the lunar Nearside has the highest multi-year average DTE communications of 96%.

B. Medium Horizon Mask Results

Based on the coarse map results, 31 Medium resolution maps were generated at 40-meter resolution for the lunar South pole. These smaller 2 km x 2 km areas covered all the coarse map illumination peaks having greater than 80% multi-year average solar illumination. Locations in 17 of the 31 Medium resolution maps had multi-year average solar illumination peaks greater than 80%. Some solar illumination peaks that are likely Digital Elevation Model processing anomalies were not considered in the final analysis. Table 2 is a summary of the best multi-year average solar illumination peaks from the medium resolution maps.

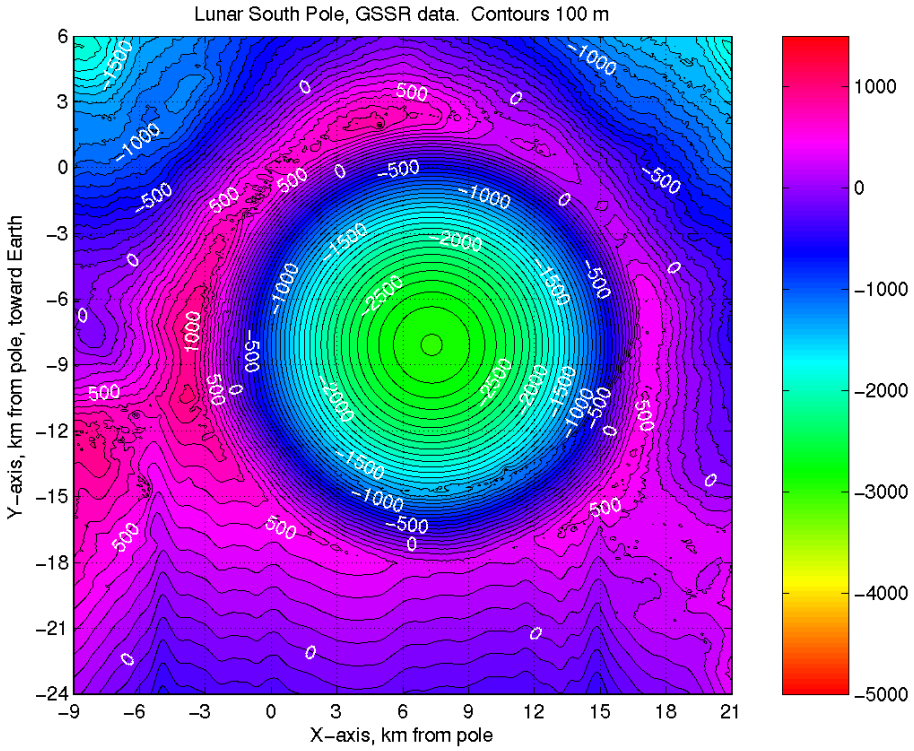

Figure 13. Shackleton Crater Elevation Topography.

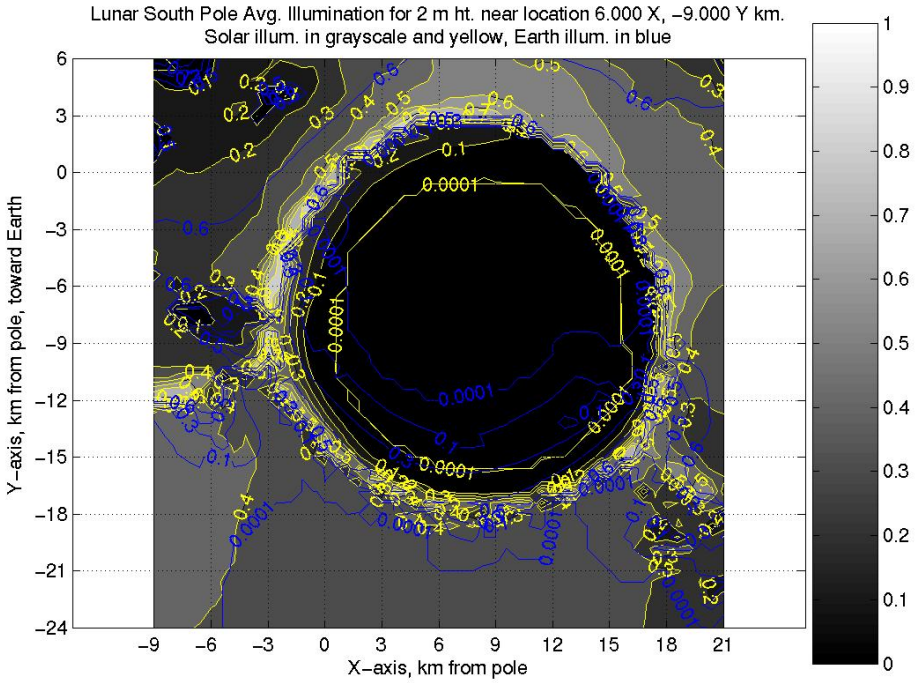

Figure 14. Shackleton Crater Yearly Average Illumination, Coarse Resolution.

The two peaks with the highest multi-year average solar illumination are shown in figures 15 through 18 in 2km X 2km maps. Figures 15 and 16 show the maximum for peak A1. Figure 15 shows the topographic elevation contours for the map centered on (-4, -10) on Shackleton crater's West rim. Figure 16 is the same area covered with multi-year average solar illumination contours every 10% and at 0.0001%. Figure 16 also shows multi-year average Earth illumination contours at 0.0001, 0.1, 0.3, 0.5, 0.6, and 0.7%. The illumination data are for any part of the disk visible, or the "0% of solar/Earth disk visible" multi-year average illumination. Figures 17 and 18 show the multi-year average contours for peak B1.

The following conclusions were made from examining these illumination peaks and the multi-year average solar illuminations and DTE maps:

1) The multi-year average solar illumination maximums occur on the highest peak in the map areas. This is expected, since taller peaks have the least obstructed views of the Sun.

2) At 40-meter resolution, the data show several grid points next to each illumination maximum peak with nearly the same multi-year average solar illumination value. This implies the peaks are spread over several pixels. This could also happen because the Digital Elevation Model data set was made self-consistent by smoothing.

3) Within a 2km x 2km area, there can be several small peaks with greater than 80% multi-year average solar illumination. An area 100's of meters across may surround the actual maximum peak that also has nearly 80% multi-year average solar illumination.

4) Multi-year average Earth visibility is also maximized on the highest peaks in the site.

5) Small changes in the terrain slope (as shown in the topographic maps) greatly reduce the multi-year average solar illumination, even within 100's of meters of the solar maximum peaks. This implies that finding solar maximum peaks using spacecraft pictures of illuminated terrain may be problematic. The conditions may mix light and dark terrain pixels in spacecraft pictures, even during the mid-Summer days. This also indicates the solar maximum peaks may not be visible on photographs due to shallow Sun angles.

6) The highest site within a region will have the greatest multi-year average solar illumination. For instance, Site B1 and B3 are located on two broad plateaus about 8 km apart. But Site B1 is about 300 meters higher, and has significantly higher multi-year average solar illumination.

Based on these observations, Sites C1 and F from Reference 4 deserved further investigation. The peaks of the two tallest mountains near the pole (Malapert α and Leibnitz β) were also added to the list, as sites MA and LB. The Coarse map peaks that were labeled Site B2 and a processing artifact peak near A4 were dropped from consideration. A fine resolution horizon mask was computed for the highest elevation point of each site.

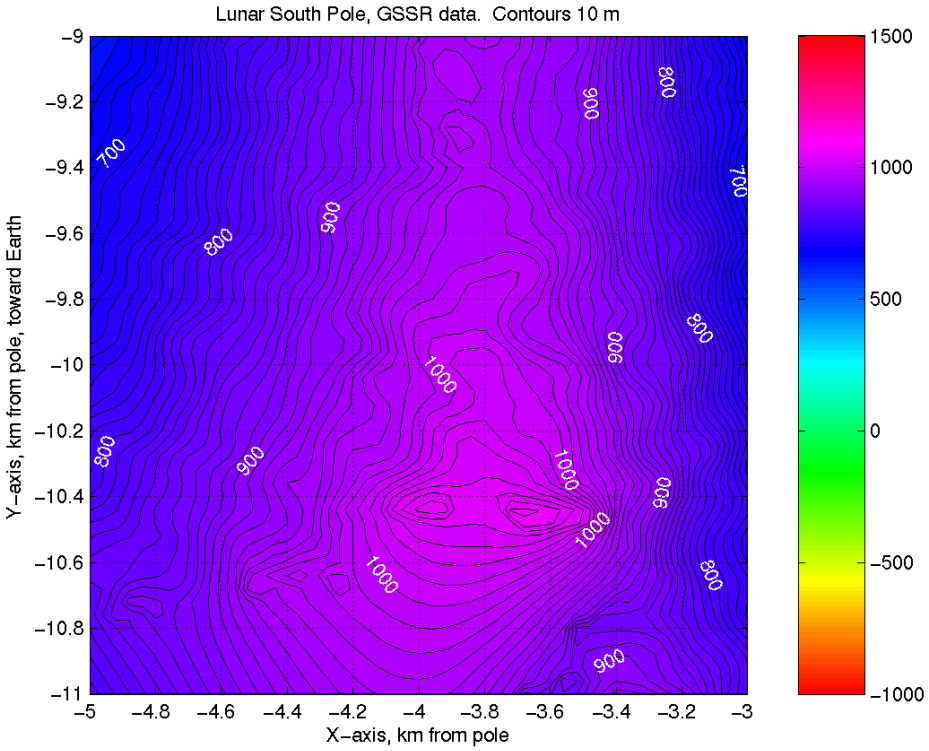

Figure 15. Site A1 Elevation Topography.

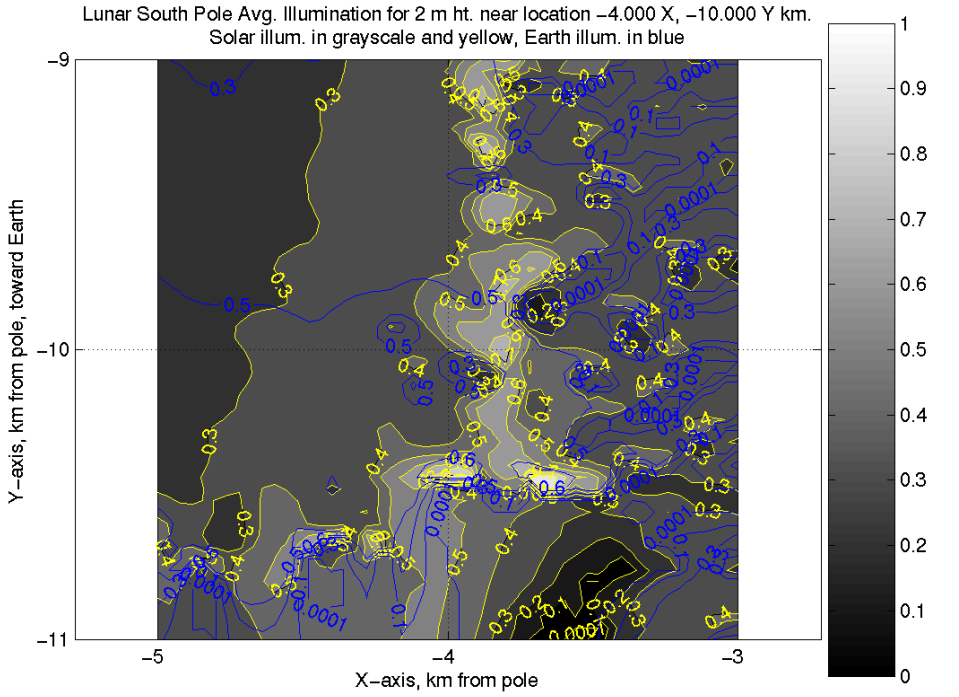

Figure 16. Site A1 Yearly Average Illumination, Medium Resolution.

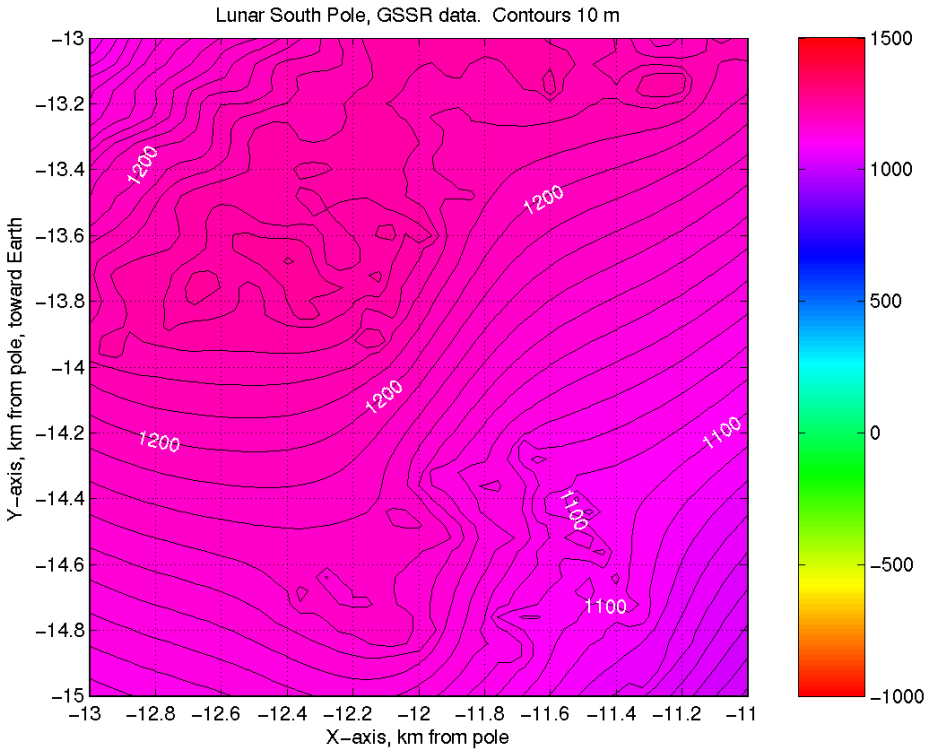

Figure 17. Site B1 Elevation Topography.

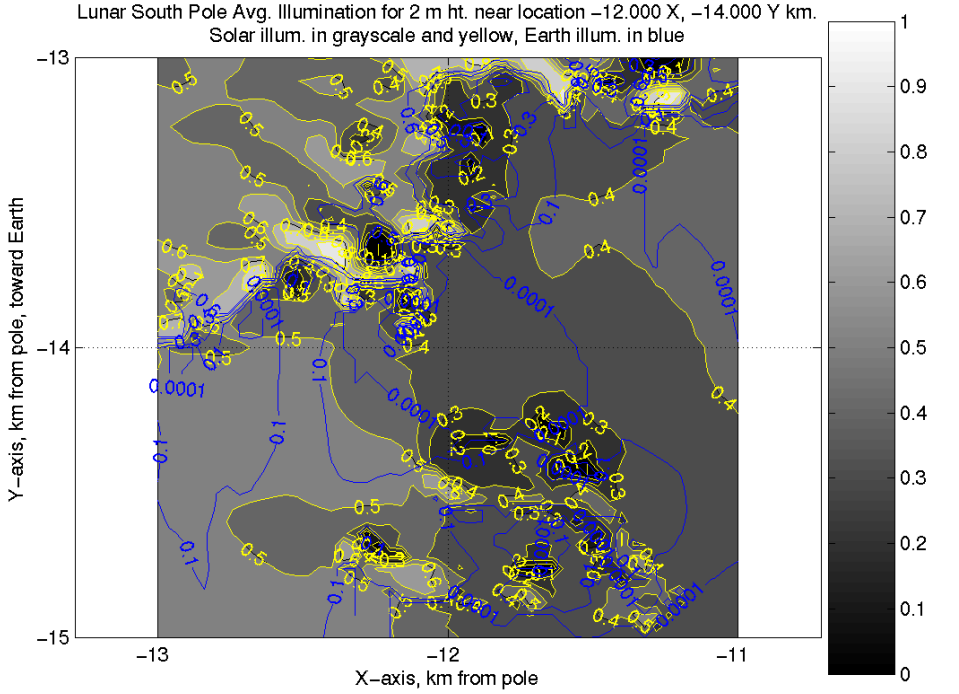

Figure 18. Site B1 Yearly Average Illumination, Medium Resolution.

Table 2. Medium View Multi-Year Average Solar Illumination Peaks Selected for Fine Resolution Analysis.

Map center, X, Y km	Site Peak	X, km	Y, km	Lat., degrees	Long., degrees	Elevation, meters	Solar illum., %	Earth illum., %
-4, -10	A1	-3.72	-10.44	-89.633	-160.388	1071.74	95.58	62.49
-4, -8	A2	-3.68	-7.52	-89.723	-153.925	1050.05	94.20	63.89
-2, -4	A3	-2.20	-3.56	-89.861	-148.285	897.49	88.93	63.41
4, 2	A4	3.72	1.92	-89.861	62.700	896.57	91.46	63.99
-12, -14	B1	-12.40	-13.68	-89.388	-137.810	1260.93	97.52	65.10
-20, -10	B3	-19.96	-10.04	-89.260	-116.703	1003.61	88.63	65.52
16, -14	H	16.52	-13.08	-89.302	128.371	631.43	84.22	64.89
	C1	-38.24	13.40	-88.657	-70.688	1143.8		
	F	28.76	-21.36	-88.813	126.601	947.4		
	Malapert α, MA	3.56	119.60	-86.037	1.704	4206.8		
	Leibnitz β, LB	101.32	123.04	-84.722	39.470	6054.5		

C. Fine Horizon Mask Results

Fine resolution horizon masks were computed for 11 site locations in the lunar South pole region. Based on the Coarse map results, 4 sites locations from the lunar North pole were added to the fine resolution analysis list. The results for the 15 sites are shown in tables 3 and 4.

The sites A1, A2, and B1 have the highest multi-year average solar illumination for the lunar South pole sites. The other Southern peaks do not have solar illumination metrics as good as these three peaks, primarily because of lower elevation. Site C1 is higher than sites A1 and A2, but is much farther from the South pole and therefore gets less average solar illumination.

The lunar North pole 'fine resolution' analysis used the same azimuth resolution as the lunar South pole analysis (1 degree steps), but was performed using 600-meter resolution data. The 4 Northern sites in Tables 2 and 3 are Sites NA, NB, NC, and NG. The sites NB and NC have higher multi-year average solar illumination than the lunar South pole sites, primarily because there are no obscuring peaks as tall as Malapert α and Leibnitz β at the lunar South pole.

At the lunar South pole, Site B1 has the highest average yearly solar illumination of 97%. Site B1 also has an average Earth visibility (65%) higher than the nearby sites A1 through A4. Site B1 has the most months of continuous solar illumination, with some part of the solar disk visible during 8 synodic months. The solar power generation metrics show site B1 has the lowest total days of darkness, during the Winter month, for these 5 sites. However, sites A1 and A2 have shorter total days of continuous darkness, during the Winter month, than site B1. This could be significant when selecting the base locations, since it directly affect the battery storage sizing for the base.

These solar illumination statistics are for multi-year averages of the solar motion. This allows valid site-to-site comparisons, but doesn't provide information for the solar illumination on specific dates.

Table 3. Fine resolution Solar Illumination Statistics.

			Multi-year average illumination			months 100% visible			days dark in Winter month			days longest continuous darkness		
			(% of Sun visible)			(% of Sun visible)			(% of Sun visible)			(% of Sun visible)		
Site	X,km	Y,km	(0)	(50)	(100)	(0)	(50)	(100)	(0)	(50)	(100)	(0)	(50)	(100)
A1	-3.720	-10.440	93.46	90.36	86.31	4.05	2.98	1.92	8.94	12.06	15.99	2.46	2.71	5.50
A2	-3.680	-7.520	92.98	89.47	84.83	4.46	3.40	2.34	10.58	13.70	18.29	2.63	2.79	3.04
A3	-2.200	-3.560	85.36	80.75	75.22	0.05	0.00	0.00	14.03	18.37	20.43	4.92	8.86	9.19

A4	3.720	1.910	87.83	83.66	78.51	0.00	0.00	0.00	13.21	17.06	19.85	6.23	7.63	9.92
B1	-12.400	-13.680	97.01	94.79	91.67	8.02	6.96	5.90	6.32	9.59	11.73	2.79	4.10	7.54
B3	-19.960	-10.040	83.84	80.50	76.55	0.00	0.00	0.00	11.56	14.19	16.07	6.89	7.05	10.09
H	16.520	-13.080	77.53	72.20	66.57	1.60	0.53	0.00	17.39	18.95	19.85	10.42	10.74	13.78
C1	-38.240	13.400	90.01	86.95	83.12	4.29	3.23	2.17	9.27	12.22	13.94	5.33	5.90	11.31
F	28.760	-21.360	89.28	85.97	81.77	4.13	3.06	2.00	10.09	12.87	15.25	5.90	6.39	8.94
MA	3.560	119.600	82.08	78.36	74.49	0.88	0.00	0.00	12.62	12.86	13.93	12.62	12.86	13.18
LB	101.320	123.040	79.06	77.43	75.82	0.00	0.00	0.00	9.15	9.48	9.72	9.15	9.48	9.72
NA	-7.800	-7.200	94.52	89.83	83.70	5.46	4.39	3.33	12.88	18.70	23.79	3.69	12.14	12.30
NB	4.200	2.400	97.51	94.01	88.11	7.39	6.33	5.27	8.12	15.67	23.38	3.12	4.92	6.23
NC	15.000	13.200	98.36	96.19	92.73	8.99	7.93	6.87	5.58	8.94	15.34	1.56	3.61	8.77
NG	12.600	-89.400	86.56	83.16	79.64	4.44	3.37	2.31	11.39	11.80	12.37	11.39	11.80	12.29

Table 4. Fine resolution Earth Visibility Statistics.

			Multi-year average DTE Communications		
			(% of Earth visible)		
Site	X, km	Y, km	(0)	(50)	(100)
A1	-3.720	-10.440	62.20	55.29	48.37
A2	-3.680	-7.520	63.90	56.98	50.07
A3	-2.200	-3.560	63.41	56.50	49.58
A4	3.720	1.910	63.97	57.06	50.14
B1	-12.400	-13.680	65.16	58.24	51.33
B3	-19.960	-10.040	65.60	58.69	51.77
H	16.520	-13.080	62.02	55.11	48.20
C1	-38.240	13.400	70.97	64.05	57.14
F	28.760	-21.360	67.30	60.38	53.47
MA	3.560	119.600	100.00	100.00	94.68
LB	101.320	123.040	100.00	100.00	100.00
NA	-7.800	-7.200	70.82	63.91	57.00
NB	4.200	2.400	66.89	59.98	53.07
NC	15.000	13.200	66.18	59.27	52.35
NG	12.600	-89.400	96.15	91.62	85.37

The multi-year average Earth visibility metrics of Table 4 indicate little variation between the sites on the rim of Shackleton Crater. In general, the best visibility to some part of the Earth is around 65% for the lunar Polar Regions. From these peaks, the entire Earth is visible about 50% of the sidereal month. Therefore, continuous polar lunar base coverage requires some kind of Earth relay. The sites on the peaks of Malapert α and Leibnitz β have 100% visibility of Earth at all times. These sites also have direct line-of-sight to the rim of Shackleton crater. This makes possible a communications system design using a radio frequency reflector at one of these sites as a continuous relay between Earth and sites on the rim of Shackleton crater. For the lunar North pole, site NG on the North rim of Peary Crater has 96% visibility of Earth. This site could provide a nearly continuous relay between Earth and sites NB and NC near the lunar South pole.

D. Computing Metrics from Ephemeris Data

The validity of assuming a uniform distribution of solar and Earth exposure was investigated using actual ephemeris data. The location of the Sun and Earth were computed using the HORIZON ephemeris computation service provided by the Jet Propulsion Laboratory. Data files were created in selenographic latitude and longitude for the period January 1, 2009 to January 1, 2028 with 24-hour spacing. This period covered a complete18.6-year regression of the longitude of the ascending node of the moon. Ephemeris data was generated for 4 observation data sets:

1) The view of the Sun from the lunar North pole
2) The view of the Sun from the lunar South pole

3) The view of the Earth from the lunar North pole
4) The view of the Earth from the lunar South pole

This data was used to compute 4 distribution patterns in selenographic latitude and longitude. The distribution patterns show the time in hours each location is covered by the Sun (or Earth) during the 19-year period. Figures 19 and 20 show the Sun distribution patterns as seen from the lunar North and South poles. Figures 21 and 22 show the Earth distribution patterns as seen from the lunar North and South poles. The figures show the distribution pattern is not uniform. The Sun distributions are uniform in longitude and vary less than a factor of 2 from the average in latitude. The Earth distributions are approximately uniform in longitude between the + and – 4 degrees latitude. The Earth distribution does have 4 peaks almost 3.7 times the average value, but these peaks are at greater than + and – 5 degrees latitude. For site locations at the lunar poles, the 4 Earth distribution peaks are located so that 2 peaks always visible, and 2 peaks always below the horizon. This effectively cancels out the asymmetry of the Earth distribution patterns, as seen from the lunar poles.

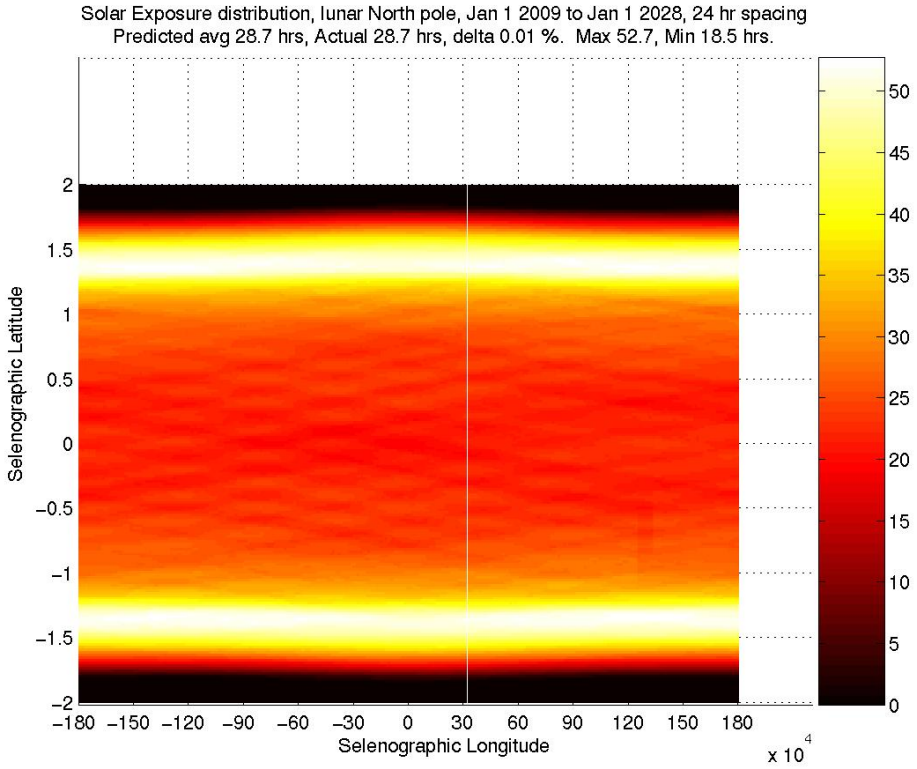

Figure 19. Solar Distribution Pattern, viewed from lunar North pole.

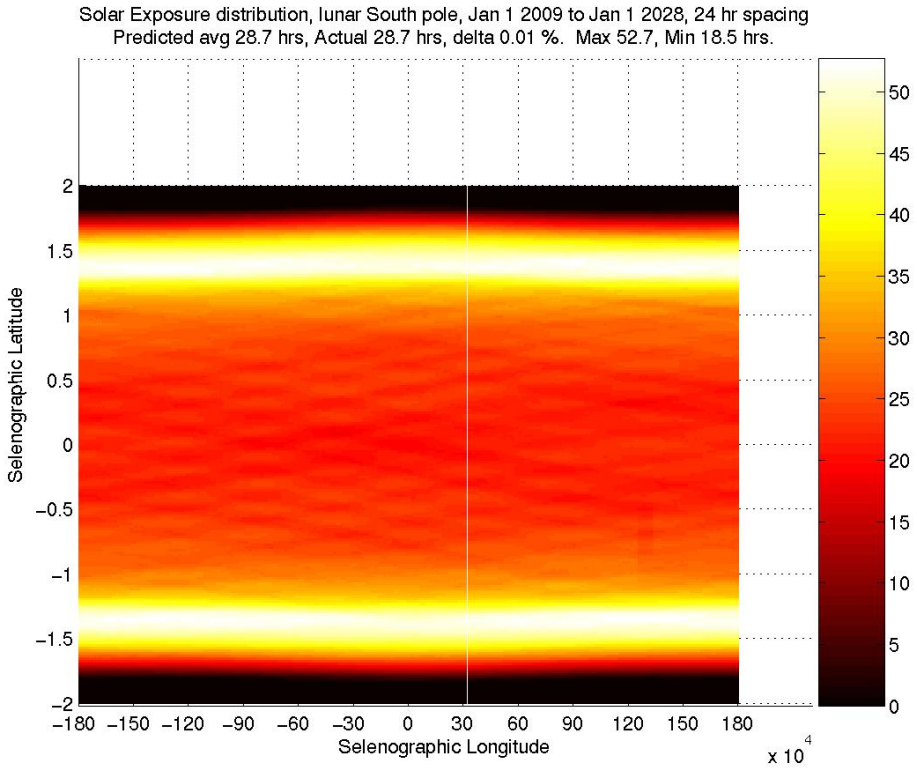

Figure 20. Solar Distribution Pattern, viewed from lunar South pole.

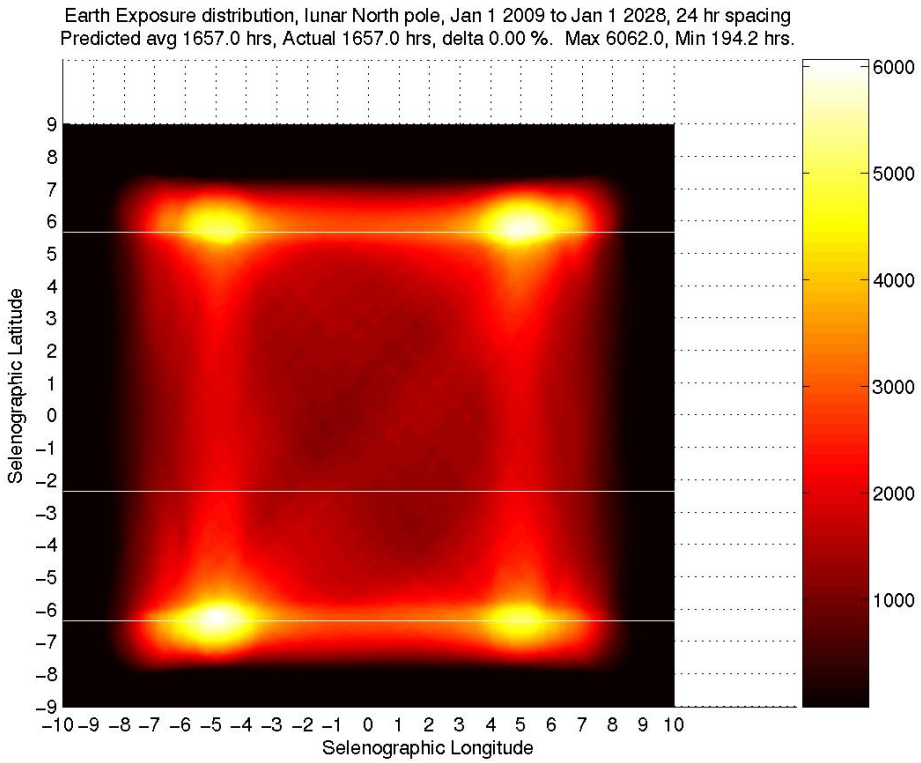

Figure 21. Earth Distribution Pattern, viewed from lunar North pole.

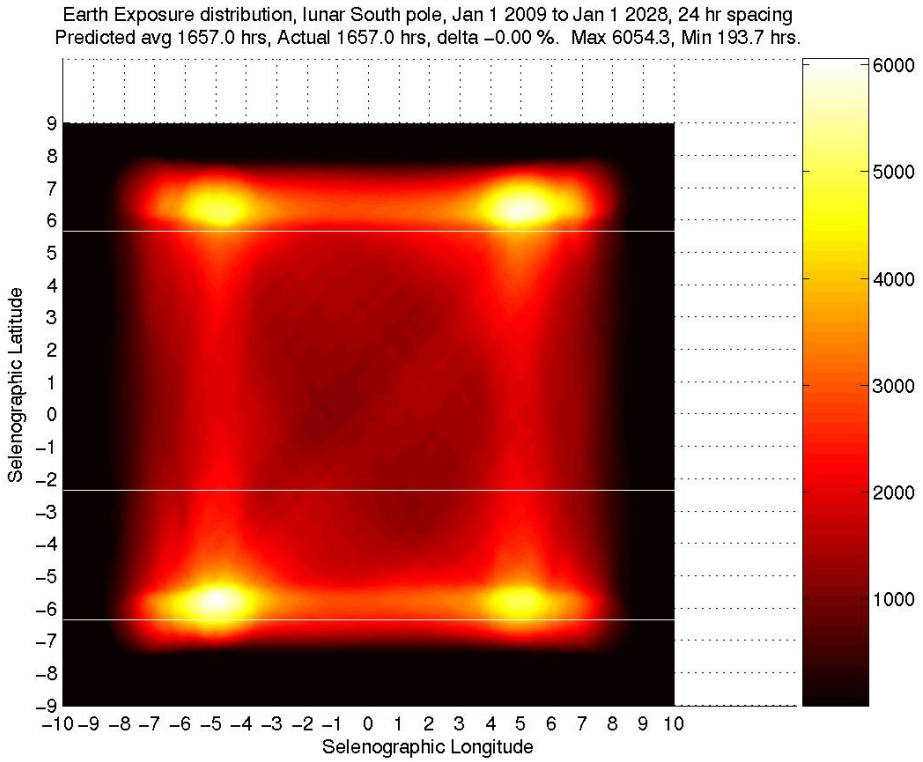

Figure 22. Earth Distribution Pattern, viewed from lunar South pole.

These distribution patterns were computed using the following algorithms. Starting with the first set of latitude, longitude, and time (lat_i , $long_i$, t_i) in an ephemeris file; compute the angular distance and time between the current point and next point with the equation:

$$L = \sqrt{\left(long_{i+1} - long_i\right)^2 + \left(lat_{i+1} - lat_i\right)^2}$$
$$T = t_{i+1} - t_i \tag{1}$$

For each point (lat, long) within R (0.95 degrees for Earth, 0.25 degrees for the Sun) of the line between (lat_i , $long_i$, t_i) and (lat_{i+1} , $long_{i+1}$, t_{i+1}), perform a coordinate transformation that maps to (lat, long) to (Y_i, X_i) and (Y_{i+1}, X_{i+1}). The coordinate X_i is the distance from (lat_i , $long_i$) along the line L between (lat_i , $long_i$) and (lat_{i+1} , $long_{i+1}$). The coordinate Y_i is the perpendicular from the line L. The coordinate X_{i+1} is the distance from (lat_{i+1} , $long_{i+1}$) along the line L and Y_{i+1} is the perpendicular from the line L. The transformation is given by:

$$
\begin{aligned}
X_i &= \left\{ (long - long_i)\frac{(long_{i+1} - long_i)}{L} + (lat - lat_i)\frac{(lat_{i+1} - lat_i)}{L} \right\} \\
Y_i &= \left\{ (lat - lat_i)\frac{(long_{i+1} - long_i)}{L} - (long - long_i)\frac{(lat_{i+1} - lat_i)}{L} \right\} \\
X_{i+1} &= L - X_i \\
Y_{i+1} &= Y_i
\end{aligned}
\tag{2}
$$

The exposure time, E, at each point (lat, long) that gets added to the distribution pattern for the ephemeris point (lat_i , $long_i$, t_i) is determined by the region the transformed coordinates (Y_i, X_i) and (Y_{i+1}, X_{i+1}) occupy. The 5 regions are given by:

$$
\begin{aligned}
&[1],\ \left(X_i^2 + Y_i^2 < R^2\right) and\ \left(X_{i+1}^2 + Y_{i+1}^2 < R^2\right) \Rightarrow E = T \\
&[2],\ Not\ in\ [1]\ and\ \left(X_i^2 + Y_i^2 < R^2\right) \Rightarrow E = \frac{T}{L}\left(X_i + \sqrt{R^2 - Y_i^2}\right) \\
&[3],\ Not\ in\ [1]\ and\ \left(X_{i+1}^2 + Y_{i+1}^2 < R^2\right) \Rightarrow E = \frac{T}{L}\left(X_{i+1} + \sqrt{R^2 - Y_{i+1}^2}\right) \\
&[4],\ Not\ in\ [2][3]\ and\ \left(Y_i < R\right) and\ \left(X_i > 0\right) and\ \left(X_i < L\right) \Rightarrow E = \frac{2T}{L}\sqrt{R^2 - Y_i^2} \\
&[5],\ Not\ in\ [2][3][4] \Rightarrow E = 0
\end{aligned}
\tag{3}
$$

The summation of E over all the points (lat, long) for each data point in an ephemeris file produced a distribution pattern for the time interval of the ephemeris. The results from the 4 ephemeris data sets were used to produce figures 19 through 22. The distribution pattern was also used in place of the original uniform distribution to produce new fine resolution metrics as described in section 3.4. The ephemeris distributions were used to compute the fine resolution metrics shown in blue in figures 6, 23, 24, 25, and 26 for the lunar pole sites B1, C1, MA, NC, and NG. The metrics show an agreement better than 5% between the metrics based on a uniform distribution, and the metrics based on the ephemeris distribution from 2009 to 2028.

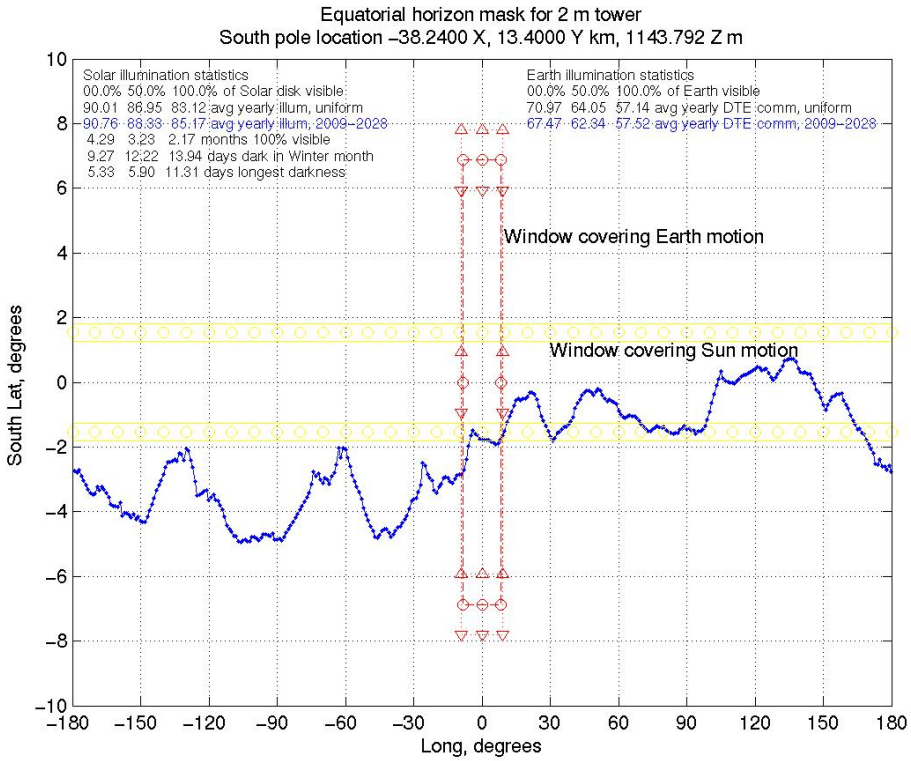

Figure 23. Site C1 Terrain horizon mask, 1 degree azimuth steps, in selenographic coordinates.

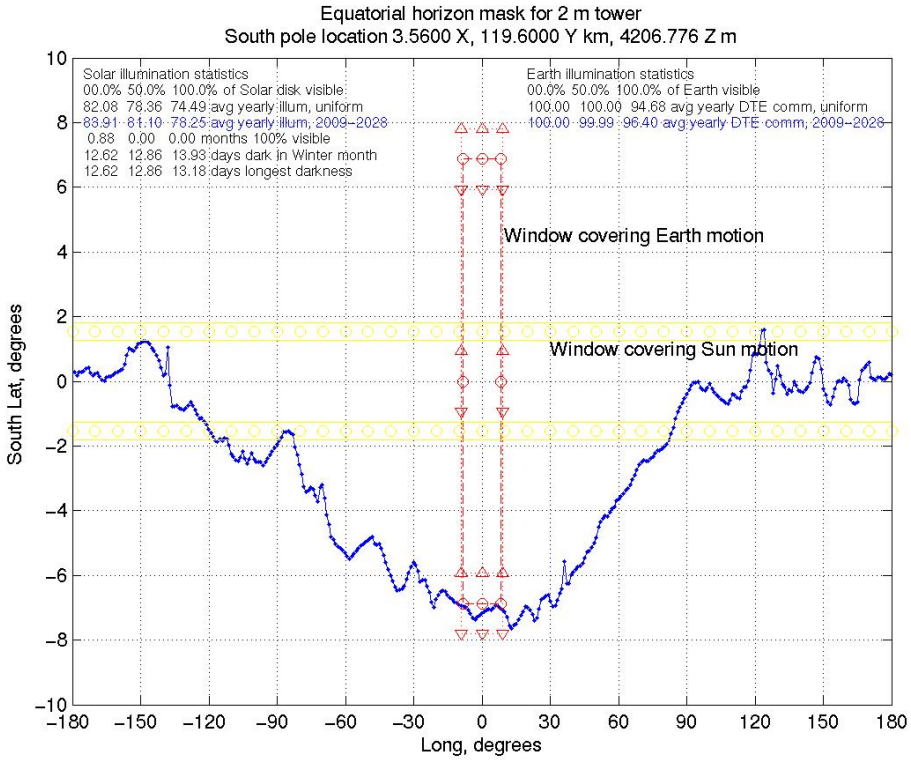

Figure 24. Site MA Terrain horizon mask, 1 degree azimuth steps, in selenographic coordinates.

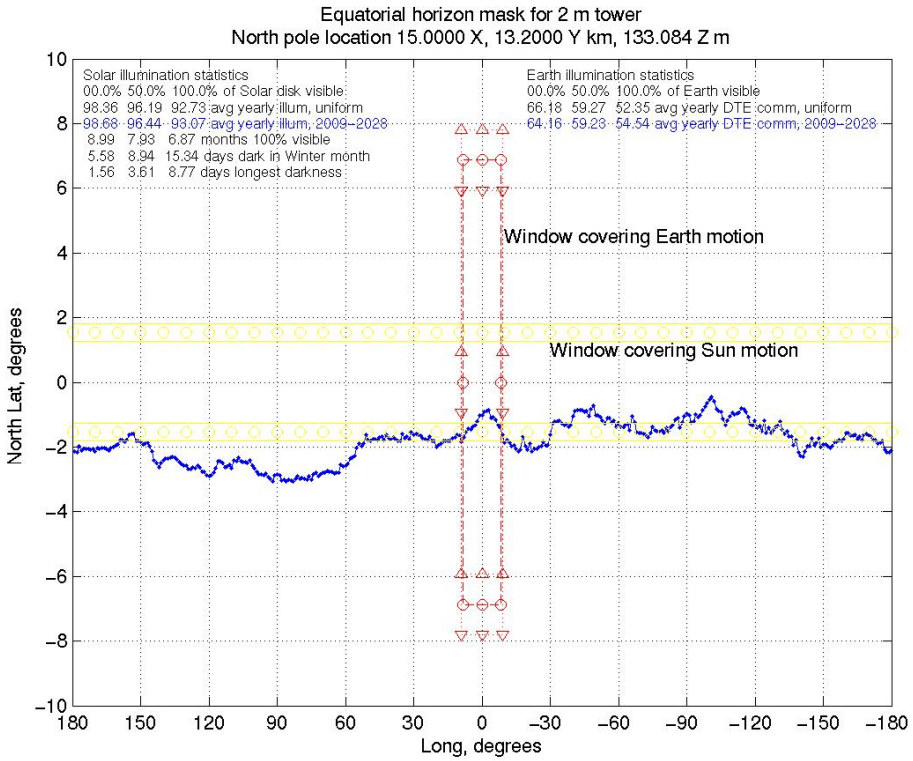

Figure 25. Site NC Terrain horizon mask, 1 degree azimuth steps, in selenographic coordinates.

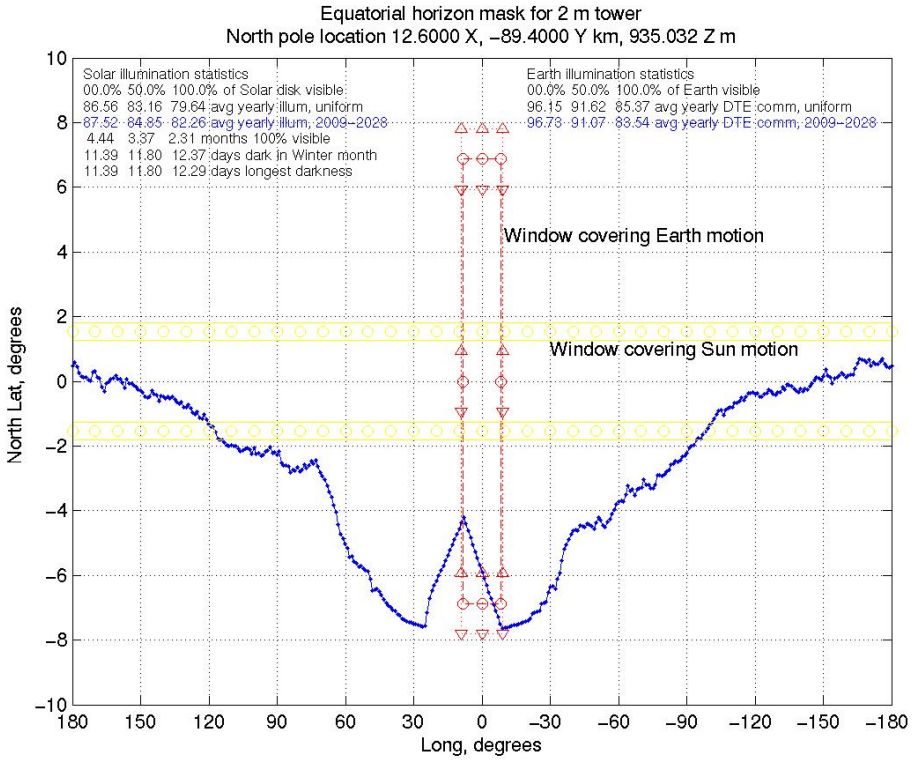

Figure 26. Site NG Terrain horizon mask, 1 degree azimuth steps, in selenographic coordinates.

E. Using Towers to Improve Metrics

Solar illumination and Earth visibility metrics increase with increased altitude above the local terrain. The following equations show this variation as a function of altitude and distance from the pole. The equations assume a spherical lunar surface of radius, R, an altitude above this surface, h, and a distance from the pole, d. The equations are written in terms of colatitude, θ, and below-the-horizon view angle, ϕ, given by the following equations.

$$\theta = \frac{d}{R} \times \frac{180}{\pi} \tag{4}$$

$$\phi = \arccos\left(\frac{R}{R+h}\right) \tag{5}$$

The multi-year average equations integrate along the local horizon, converted to lunar latitude-longitude coordinates. The derivation uses an approximation for small angles that gives Eq. (7). This equation is valid for small angles near the polar regions.

$$\begin{aligned} longitude &\approx \arccos\left(\frac{-\phi - latitude}{\theta}\right), \\ latitude &\approx -\phi - \theta\cos(longitude) \end{aligned} \tag{6}$$

Integrating the area above the horizon mask and between the solar latitude limits produced an equation for the yearly average solar illumination. The solar latitude limits are + and -1.54 degrees, represented by + and – α below. The equation uses the variables L1 for the longitude where the horizon mask crosses –α latitude, and L2 for the longitude where the horizon mask crosses +α latitude. These variables are:

$$\begin{aligned} L1 &= \begin{cases} if\ (\theta+\phi) \geq \alpha, & \arccos\left(\dfrac{-\phi+\alpha}{\theta}\right) \\ else, & 0 \end{cases} \\ L2 &= \begin{cases} if\ (\theta-\phi) \geq \alpha, & \arccos\left(\dfrac{-\phi-\alpha}{\theta}\right) \\ else, & 180 \end{cases} \end{aligned} \tag{7}$$

The multi-year average solar illumination, I, is then predicted by Eq. (8):

$$I = \frac{L1}{180} + \frac{(\alpha+\phi)(L2-L1)}{360\times\alpha} + \frac{\theta}{2\pi\alpha}\left[\sin(L2) - \sin(L1)\right] \tag{8}$$

Integrating the area above the horizon mask and between the Earth latitude limits produced the multi-year average Direct to Earth communication equation. The Earth latitude limits are + and -6.87 degrees, represented by +

and –γ below. The Earth longitude limits of + and -8.16 degrees are represented by + and –β below. The equation uses the variable L0 for the longitude of the site at Cartesian coordinates (x,y) centered on the pole. The equation uses the variable L1 for the longitude where the horizon mask crosses –β latitude. These variables are given by:

$$L0 = abs\left[\arctan\left(x/y\right)\right]$$
$$L1 = \begin{cases} if\ \left(\theta+\phi\right) \geq \gamma, & \arccos\left(\dfrac{-\phi+\gamma}{\theta}\right) - L0 \\ else, & -\beta \end{cases} \tag{9}$$

The yearly average Earth communications, DTE, is then given by Eq. (10):

$$DTE = \frac{1}{4\gamma\beta}\left\{2\gamma\left(L1+\beta\right)+\left(\gamma+\phi\right)\left(\beta-L1\right)+\theta\frac{180}{\pi}\left[\sin\left(\beta+L0\right)-\sin\left(L1+L0\right)\right]\right\} \tag{10}$$

Comparing these theoretical equations with the computed illumination and DTE communications averages required using an adjusted lunar reference altitude at the poles. The lunar reference geoid radius of 1738 km is not a good average value for the terrain at either pole. The lunar South pole is part of the Aitken Basin, and the GSSR Digital Elevation Model elevations have an average of -1880 m within 200 km of the South pole. The lunar North pole region has an average elevation of -1673 m within 150 km of the North pole. These averages were subtracted from base site reference altitude to get the value of 'h' used in equation 2. This effectively gives the base sites a higher elevation relative to the local average elevation.

For selected base sites, solar illumination and DTE communications averages were computed for tower heights from 2 m to 1500 m, and in some cases 3000 m. Fine resolution metrics were produced from the assumed uniform sun and Earth distributions, and from the distribution patterns produced from the 2009 to 2028 ephemeris data.

Table 5 show multi-year average metrics for site B1 near the lunar South pole at (X, Y) location (-12.400 X km, -13.680 Y km) and elevation 1261 meters. The table shows metrics for tower heights from 2 meters to 3000 meters above the base surface elevation.

Table 5. Solar Illumination Metrics for Site B1 Tower Heights.

Tower height	Solar illumination statistics, Assumed uniform distribution Multi-year average illumination			Solar illumination statistics, Distribution from 2009 to 2028 Multi-year average illumination		
meters	(0%)	(50%)	(100%)	(0%)	(50%)	(100%)
2.0	97.01	94.79	91.67	97.08	94.89	91.99
4.0	97.11	94.91	91.81	97.21	95.02	92.12
8.0	97.24	95.08	91.99	97.36	95.21	92.30
16.0	97.42	95.35	92.29	97.52	95.49	92.61
32.0	97.60	95.67	92.69	97.71	95.79	93.03
64.0	97.89	96.15	93.41	97.98	96.27	93.78
128.0	98.21	96.79	94.56	98.25	96.90	94.91
256.0	98.56	97.46	95.74	98.57	97.53	95.96
500.0	98.90	98.14	96.90	98.90	98.09	97.07
1000.0	99.38	98.72	97.93	99.48	98.70	97.89
1500.0	99.76	99.23	98.54	99.85	99.29	98.49
2000.0	99.95	99.65	99.06	99.98	99.74	99.10
2500.0	100.00	99.89	99.51	100.00	99.95	99.60
3000.0	100.00	99.99	99.81	100.00	100.00	99.88

Table 6 shows the multi-year average metrics for a uniform Earth distribution and the actual Earth distribution pattern produced from the 2009 to 2028 ephemeris data.

Table 6. Earth Illumination Metrics for Site B1 Tower Heights.

Tower height	Earth DTE statistics, Assumed uniform distribution Multi-year average illumination			Earth DTE statistics, Distribution from 2009 to 2028 Multi-year average illumination		
meters	(0%)	(50%)	(100%)	(0%)	(50%)	(100%)
2.0	65.16	58.24	51.33	63.47	58.61	53.95
4.0	65.16	58.25	51.33	63.48	58.61	53.96
8.0	65.17	58.26	51.35	63.49	58.62	53.97
16.0	65.20	58.29	51.37	63.51	58.63	53.98
32.0	65.25	58.34	51.42	63.54	58.67	54.01
64.0	65.35	58.44	51.52	63.61	58.74	54.08
128.0	65.56	58.64	51.73	63.75	58.88	54.21
256.0	65.96	59.05	52.13	64.04	59.14	54.47
500.0	66.74	59.82	52.91	64.60	59.66	54.97
1000.0	68.32	61.41	54.50	65.74	60.73	56.00
1500.0	69.91	63.00	56.08	66.91	61.81	57.03
2000.0	71.48	64.56	57.65	68.10	62.91	58.07
2500.0	73.04	66.12	59.21	69.33	64.01	59.12
3000.0	74.58	67.67	60.76	70.58	65.14	60.17

For the 2 distribution patterns, the same solar illumination metric agrees within 1%. For the 2 distribution patterns, the same Earth visibility metric agrees within 5%. This level of agreement validates the simplifying assumption of uniform sun and Earth distributions over the bounding latitude and longitude regions.

These tower heights, plus adjusted altitudes and base locations, were used in equations 4 through 10 to get predicted values of the multi-year average metrics. The results are shown in figures 27 and 28. Figure 27 shows black curves of Eq. (8) plotted parametrically with distance from the pole. For the selected sites, the computed multi-year average solar illumination (assuming a uniform distribution) is shown by squares, connected by a dashed line with the theoretical yearly average for the same location and tower heights. The theoretical values are marked with X's. The computed multi-year average solar illumination (for ephemeris data from 2009 to 2028) are marked with +'s. Lunar South pole sites are in blue and the lunar North pole sites are in red. The plotted values show reasonable agreement of computed values and theory, with the computed values usually less than the theoretical. Figure 28 shows black curves of Eq. (10) plotted parametrically with distance from the pole toward the Nearside. The value of L0 was set to zero for the parametric curves. Figure 28 includes computed and theoretical values of the multi-year average DTE communications for the same sites as figure 27, using the same symbol and color conventions.

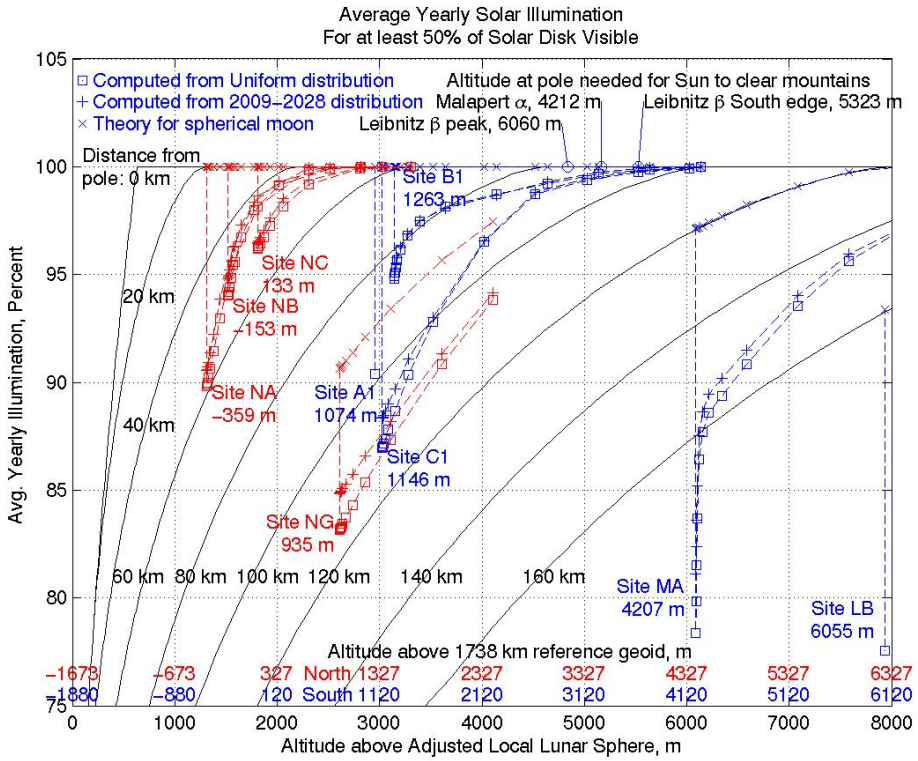

Figure 27. Theory and Computed values of Multi-Year Average Solar Illumination.

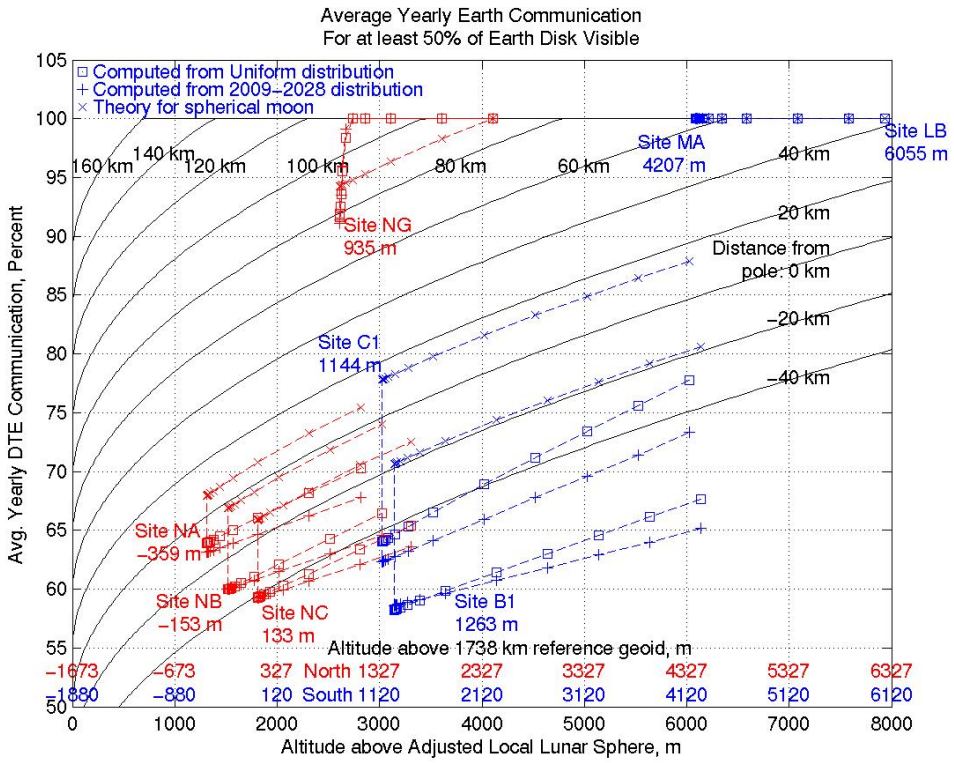

Figure 28. Theory and Computed values of Multi-Year Average DTE Communications.

No site has both 100% multi-year average solar illumination and 100% multi-year average DTE communications for a tower less than 1500 m tall. Towers of 1500 m at sites NB and NC will raise the multi-year average solar illumination to 100%. But for the lunar South pole sites, like B1, towers of over 2500 m are required to raise the multi-year average solar illumination to 100%. This is because the peaks Malapert α and Leibnitz β obscure the view of the sun from the lunar South pole. Equation (11) gives the elevation, Hp, above a spherical surface needed to see the winter sun over a peak of elevation Hm at a distance, d, from the pole. Equation (11) provided values in Figures 4 and 27 for the Malapert α and Leibnitz β peaks.

$$Hp = (R + Hm)\frac{\cos\left(\frac{180}{\pi}\frac{d}{R} - \alpha\right)}{\cos(\alpha)} - R \tag{11}$$

The obscuring effect of these peaks is also shown in figure 5, where the peak Malapert α appears at +10 degrees azimuth.

Figure 28 shows the multi-year average DTE communication varies more with distance from the pole toward the prime meridian than with tower height above the local terrain. Towers up to 3000 m at the poles do not make significant improvements in the DTE communications average. At the lunar North pole, the computed multi-year average DTE communications for site NG exceeds the predicted values for towers between 32 and 1500 meters tall. This is because the view toward lunar Nearside from site NG (at elevation 935 m) looks across the floor of Byrd Crater, which averages about -2500 m elevation.

The theory values generally correlate with the trends of the computed values, but are offset as much at 20%. This indicates that a theoretical model based on a spherical moon does not capture the true physics of the horizon masks. The average elevation of a spherical model considers peaks and valleys in the terrain, but the peak elevations are the driving force behind the horizon mask visibility metrics. However, the convergence of the computed metrics with the theoretical metrics for the tallest towers is an expected result that lends confidence to the computed results.

V. Considerations for Photovoltaic Array Design

The lunar pole sites create some difficult challenges for designing a continuously operating photovoltaic power system. The requirement to continually track the sun could be met by installing the photovoltaic array on a vertical axle, oriented parallel to the lunar spin axis. At the lunar South pole, this axle would rotate counterclockwise with the sun to keep the array normal to the solar radiation. This requires a foundation to support the axle, cross beam structures to hold the array on the axle, and a drive system powerful enough to turn the array. This system also requires a solution to the 'cable wrap' problem, in order to continually track the sun. After 1 synodic month the array has turned through 360 degrees, and needs to continue rotating in the same direction. There are two basic approaches to this problem:

1) The 'slip ring' solution: Power and control cables from the array go through multiple slip rings between the rotating array and the lunar surface. The design is complicated by the requirement to tolerate the fine dust on the lunar surface.

2) The 'cable unwrap' solution: The array is rotated 360 degrees clockwise to unwrap the cables. Using the method means stopping power production for a short amount of time, once per synodic month.

A heliostat design using a focusing mirror may provide a solution to the 'cable wrap' problem[10]. This heliostat design may also produce a power system with lower mass than the other designs, because it does not need to support a rotating photovoltaic array. Figure 29 shows show the heliostat design with the photovoltaic array installed horizontal to the local terrain. A parabolic mirror is installed above the array, angled at approximately 45 degrees to the local horizontal. This mirror is suspended from the crossbar of a mast placed next to the array. The mast could also be the structure for the Lunar Communications Terminal (LCT) antennas. The mirror is suspended from an axle that is oriented parallel to the lunar spin axis. This axle rotates once per synodic month to continually reflect solar radiation onto the array. The mirror can continue to track the sun after 360 degrees revolution, since there are no cables attached to the moving part. This heliostat 'periscope' design provides continuous solar tracking, but is partially shaded once per revolution when the sun passes behind the support mast.

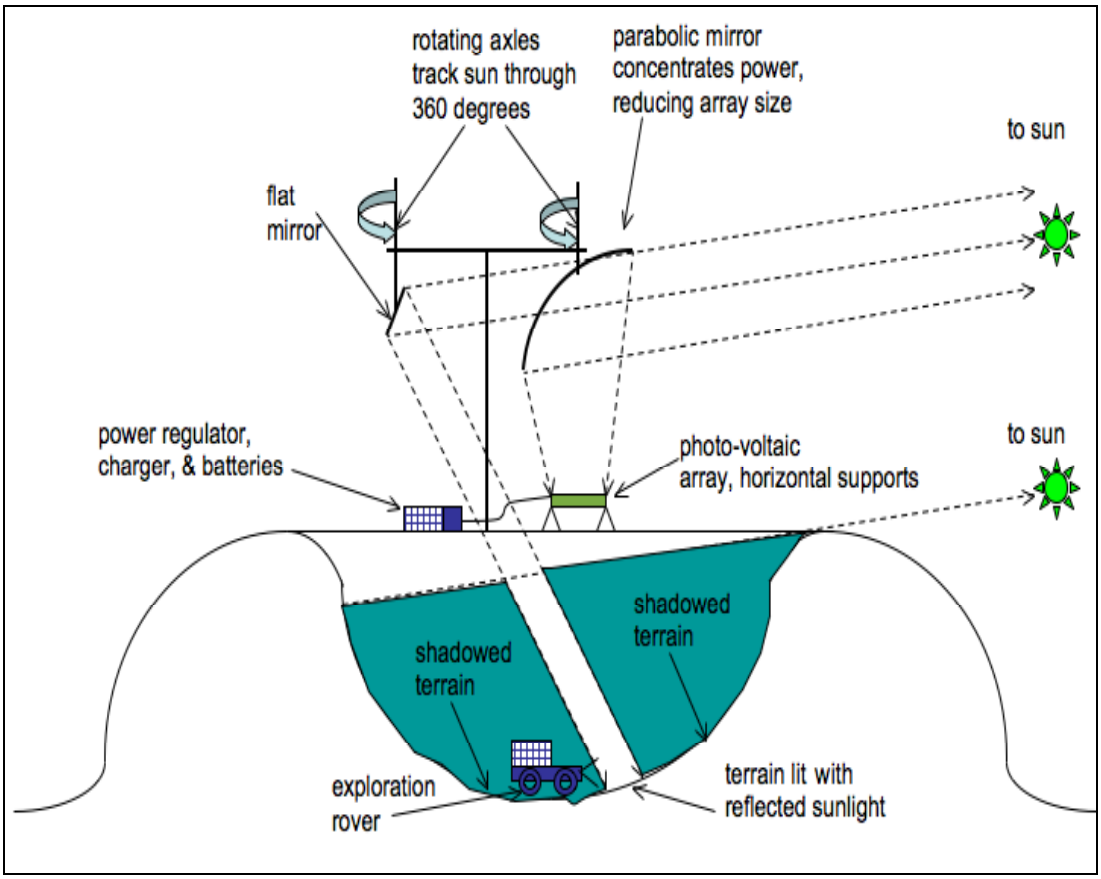

Figure 29. Periscope Mirror Design to Eliminate Cable Wrap.

Shaping the mirror into a parabolic arc concentrates solar power for a small increase in mass. The tradeoffs should consider the relative mass-per-unit area of the mirror and the photovoltaic panels, the reflectivity of the mirror material, and the relative masses of a rotating axle that supports the photovoltaic array versus supporting a mirror.

Additional flat 'periscope' mirrors mounted on the crossbar could be used to direct solar light to areas nearby. This provides an efficient method of lighting work areas because it bypasses the inefficiencies of the photovoltaic system, battery storage, and electric lighting. If the photovoltaic power system is located on a crater rim (as in Figure 29), a flat 'periscope' mirror could provide continuous lighting to exploration crews in the permanently shadowed areas within the crater. Sufficiently large heliostat mirrors could redirect enough sunlight to run photovoltaic arrays at remote locations. This would provide very efficient power transfer for operating within the permanently shaded areas. Transferring solar power with heliostat mirrors can also extend the mission operations time in the permanently shaded areas but removing the need to return to the base for recharging batteries.

VI. Conclusions

Separating the lunar pole solar illumination problem into terrain horizon mask and solar motion computations simplified the production of illumination metrics. Using a simplified model of multi-year average solar motion allowed quick comparisons between potential human base locations at both lunar poles. The results show that within 100 km of the lunar South pole, solar illumination is maximized at previously identified Site locations[3, 4, 5].

The best Sites are on the rim of Shackleton crater, and the ridge West of Shackleton crater. These 3 Sites have multi-year average solar illumination between 90 and 97%. The Sites have 100% solar power generation capability about 85 to 91% of the year. For both of these metrics, Site B1 on the ridge West of Shackleton crater has the highest multi-year average solar illumination values. Site B1 has direct-to-Earth visibility of the entire Earth disk about 51% of each month. More detailed analysis of site B1 using the terrain horizon masks with more ephemeris

data for the years 2009 to 2028 produced metrics that agreed with the uniform distribution approximations to within 5%. Specifically, the ephemeris data showed site B1 has a multi-year average of 100% solar power generation capability about 92% of the time. The ephemeris data computed a multi-year average direct-to-Earth visibility of the entire Earth disk of about 54% of each month.

Examination of the site solar illumination profiles at 40-meter resolution shows the peaks of illumination are distributed over many points. The locations with greater than 80% solar illumination are spread over 100s of meters. This supports the conclusion that the DEM has adequate sampling to show the true terrain characteristics.

Acknowledgments

This research was carried out at the Jet Propulsion Laboratory, California Institute of Technology, under a contract with the National Aeronautics and Space Administration.

The author expresses thanks to Martin A. Slade of JPL's GSSR group for his time and assistance with the 2006 GSSR DEM data. The author also wished to thank Charles Ruggier and Laif Swanson of the SCiP Study Team at JPL for their support of this work.

References

1. J. L. Margot, D. B. Campbell, R. F. Jurgens, M. A. Slade, "Topography of the Lunar Poles from Radar Interferometry: A Survey of Cold Trap Locations", Science, Vol 284, pg 1658-1660, 4 June 1999.

2. National Aeronautics and Space Administration, "The Vision for Space Exploration", NP-2004-01-334-HQ, Feb. 2004. http://www.nasa.gov/pdf/55584main_vision_space_exploration-hi-res.pdf.

3. M. Kruijff, "The Peaks of Eternal Light on the Lunar South Pole: How they were found and what they look like", 4th International Conference on Exploration and Utilization of the Moon (ICEUM4), ESA/ESTEC, SP-462, September 2000.

4. J. Fincannon, "Lunar South Pole Illumination: Review, Reassessment, and Power System Implications", 5th International Energy Conversion Engineering Conference and Exhibit (IECEC), 25-27 June 2007, AIAA 2007-4700.

5. J. Fincannon, "Characterization of Lunar Polar Illumination From a Power System Perspective", 56th AIAA Aerospace Sciences Meeting and Exhibit, 7-10 January 2008, AIAA 2008-0447.

6. S. Bryant, "Lunar Pole Illumination and Communications Maps Computed from GSSR Elevation Data", 2009 IEEE Aerospace Conference, 7-14 March, 2009, IEEEAC paper #1659.

7. M. Zuber, I. Garrick-Bethell, "What Do We Need to Know to Land on the Moon Again?", Science, Vol 310, pg 983-985, 11 November 2005.

8. Scott Hensley, Eric Gurrola, Paul Rosen, Martin Slade, Joseph Jao, Micheal Kobrick, Raymond Jurgens, Eric De Jong, and Barbara Wilson, "Radar Generates High-Resolution Topographic Map of the Moon," Society of Photo-Optical Instrumentation Engineers News-room, June 16, 2008.

9. Ewan A. Whitaker, "The Lunar South Polar Regions", Journal of the British Astronomical Association, Vol. 64, No. 6, pp. 234-242.

10. James D. Burke, "Merits of A Lunar Polar Base Location", Lunar Bases and Space Activities of the 21st Century. Houston, TX, Lunar and Planetary Institute, edited by W. W. Mendell, 1985, p.77.